IMAGING BACTERIAL INTERACTIONS WITH SMALL OBJECTS

by

KENTARO E. HOEGER

A DISSERTATION

Presented to the Department of Physics
and the Graduate School of the University of Oregon
in partial fulfillment of the requirements
for the degree of
Doctor of Philosophy

September 2020

DISSERTATION APPROVAL PAGE

Student: Kentaro E. Hoeger

Title: Imaging Bacterial Interactions with Small Objects

This dissertation has been accepted and approved in partial fulfillment of the requirements for the Doctor of Doctor of Philosophy degree in the Department of Physics by:

Raghuveer Parthasarathy	Chairperson
Tristan Ursell	Advisor
Benjamín Alemán	Core Member
Michael Harms	Institutional Representative

and

Kate Mondloch	Interim Vice Provost and Dean of the Graduate School

Original approval signatures are on file with the University of Oregon Graduate School.

Degree awarded September 2020

DISSERTATION ABSTRACT

Kentaro E. Hoeger

Doctor of Philosophy

Department of Physics

September 2020

Title: Imaging Bacterial Interactions with Small Objects

Microbes have been found to inhabit a myriad of natural and artificial environments on earth, many of which are chemically complex and physically anisotropic – such as wet soils, the oceans, or mammalian guts. In order to navigate these environments many bacteria rely on self-propulsion to expand their colonies or traverse chemical gradients. While swimming through these viscous environments, they encounter physical anisotropies such as other swimming cells, and steric objects across a wide range of sizes.

At high densities, bacteria display behaviors which are distinct from dilute individual motion and are often better described by the collective motion of the bulk population yet are defined by the motion of individuals within the bulk. In natural systems, inter-species and intra-species diversity is the norm within cell populations. To study the effects of phenotypic diversity, we imaged the collective motion of wild-type *Bacillus Subtilis* with varied concentrations of a non-motile mutant doped into the population. We observed a transition from turbulent behavior to constrained semi-ballistic motion as the fraction of non-motile cells increased and found evidence for a non-linear relation between mean cell speed and the fraction of non-motile cells.

Swimming bacteria couple hydrodynamically to large, flat planar and low-curvature convex surfaces that create an attractive force that deviates their trajectories.

Current hydrodynamic models reproduce this behavior but their validity when considering small obstacles is unknown. We developed a novel method for the fabrication of microfluidic devices to overcome key limits presented by classic 'soft lithography' devices to image hundreds-of-thousands of high-curvature scattering interactions between swimming bacteria and micro-fabricated pillars with radii from ~ 1 to ~10 cell lengths. The results of these interactions were poorly described by current hydrodynamic models but well-fit by a sterics-only model we developed. Thus, we conclude that on these length scales cell-surface interactions are primarily steric and as curvature decreases, hydrodynamics begins to play an increasingly important role. We also observed cell motion in triangular arrays of such pillars and found that at high density, these pillars tightly constrained the direction of motion highlighting the importance of obstacle placement in their effects on cell motility.

CURRICULUM VITAE

NAME OF AUTHOR: Kentaro E. Hoeger

GRADUATE AND UNDERGRADUATE SCHOOLS ATTENDED:

University of Oregon, Eugene, OR
University of Colorado, Boulder CO

DEGREES AWARDED:

Doctor of Philosophy, Physics, 2020, University of Oregon
Bachelor of Arts, Physics, 2012, University of Colorado, Boulder

AREAS OF SPECIAL INTEREST:

Microfluidics
Microfabrication
Bacterial motility

PROFESSIONAL EXPERIENCE:

Graduate Research Assistant, Ursell Lab, University of Oregon, Eugene, Oregon, 2014-2020

Graduate Teaching Fellow, Department of Physics, University of Oregon, Eugene, Oregon, 2013-2020

GRANTS, AWARDS, AND HONORS:

PUBLICATIONS:

B. Rhodeland, K. Hoeger, and T. Ursell, "Bacterial surface motility is modulated by colony-scale flow and granular jamming," *Journal of The Royal Society Interface*, vol. 17, no. 167, p. 20200147, Jun. 2020, doi: 10.1098/rsif.2020.0147.

ACKNOWLEDGMENTS

My advisor Tristan Ursell for guiding me through the process. My lab mates Ben Rhodeland, Daniel Shoup, and Nick Lowery for all their help. Benjamin Aleman, Kara Zappitelli, Andrew Blaikie, and David Miller for all their help in microfabrication. Kurt Langworthy, Valerie Brogden, and Fuding Lin at CAMCOR for their help in characterizing and fabricating the devices. My friends Savannah Logan, Haley Palamos, Jordan Palamos, Carrie Levinn, and Amelia Rhodeland for helping me create an excellent space to live. My friends and colleagues in my cohort, and beyond. My cousins and family Dan, Drew, Katie, Mary, and Karl Volz for their support over the years. My parents Dan and Yumiko Hoeger and my sister Marie Hoeger for supporting me and pushing me through my entire life. Finally, my parter Ariel Steele who has supported me through the last five years and helped me grow.

TABLE OF CONTENTS

Chapter Page

LIST OF FIGURES

Figure Page

Figure Page

CHAPTER I

BACTERIAL MOTILITY, INDIVIDUAL AND COLLECTIVE

1.1 Introduction

It is estimated that there are 10^{31} bacteria living on Earth comprising roughly 5 x 10^{14} *kg* of carbon making their biomass on par with that of plant life [1]. Bacteria are ubiquitous microorganisms found in all environments that host life, from soils [2], [3], to oceans [4], [5], to human-fabricated systems [6], and even within larger organisms [7]–[9]. They play fundamental roles in these ecosystems providing sources of nutrients or influencing host-organism health [10]. Many bacteria explore their complex habitats using self-propulsion to expand into new environments and find recourses. Motility, in particular flagellar motility, can play a crucial role in the large-scale effects bacteria have on systems they inhabit such as invasion and infection of hosts via medical equipment [11], [12] or driving the sequestration of carbon from the atmosphere into the ocean via attractive motion towards particles [13]. Bacteria often interact in dramatic ways with attributes of the environments they are exploring, whether that be chemotaxis, the attraction toward higher nutrient concentrations [14]; rheotaxis, directed motion due to bulk fluid flow [15]; attraction to and/or collision with surfaces [16], [17]; or swarming in high-density populations of cells [18]. Understanding the physical response of cells to these perturbations to canonical free-fluid motility is essential to understanding how bacteria navigate their environments.

My thesis work focused on measuring interactions between bacteria and their physical surroundings by creating controlled environments in which to observe the motion of *Bacillus Subtilis* and *Escherichia Coli* bacteria. Chapter I (this chapter) broadly introduces a subset of the mechanisms underlying bacterial motility, cell hydrodynamics, and the collective motion of high-density populations of bacteria. Chapter II describes work measuring the distinct forms of motility observed in high-density, mixed-phenotype populations of motile and non-motile *B. Subtilis*. Chapter III describes the atypical microfluidic devices used in multiple chapters, contrasting the advantages and disadvantages of typical fabrication methods with the novel fabrication technique I developed to overcome limitations in typical device design. Chapter IV describes work using our atypical microfluidic devices to study the physical mechanisms underlying the interaction between bacteria and small, high-curvature convex surfaces. Chapter V examines the effects that arrays of small pillars have on cell motility. Chapter VI discusses possible future work and includes concluding remarks.

1.2 Bacterial Motility

Motion in aqueous fluid on microbial scales is characterized by low Reynolds number hydrodynamics ($\ll 1$) [19]. The Reynolds number is a dimensionless ratio of inertial forces to viscous forces for a moving body within a fluid, broadly describing whether fluid flow is expected to be laminar ($\lesssim 1$) or turbulent ($\gtrsim 1$), and does not account for any aspects of diffusion [20]. It is defined by

$$Re = \frac{uL}{\nu} \tag{1.1}$$

where u is the flow speed, L is the characteristic length (e.g. cell length, whale body length), and ν is the kinematic viscosity of the fluid ($\nu \approx 10^{-6}\, m^2/s$ for water at room temperature). High Reynolds number systems are dominated by inertial forces and thus Newtonian kinematics, and fluid motion is characterized by eddies, vortices, and other chaotic flow instabilities. Low Reynolds number systems are dominated by viscous forces that result in smooth, non-chaotic fluid motion, frequently dissipating energy so rapidly that kinematic acceleration is no longer accurately described as being proportional to force, rather force and velocity are proportional Bacterial motion ($u \approx 10^{-5}\, m/s,\ L \approx 10^{-6}\, m$) occurs at very low Reynolds number $Re \approx 10^{-5}$ meaning that inertia (and conservation of energy and momentum) is not an important kinematic concept at these scales; for a cell to be in motion, it must be actively propelling itself forward (thus expending metabolic energy) A simple kinematic calculation shows that upon ceasing to propel itself, a bacterium will come to a halt within a fraction of an angstrom.

B. subtilis and *E. coli* are both examples of pusher-type microswimmers that propel themselves by rotating multiple flagella that bundle behind the cell body and generate forward motion by moving fluid backward [21]–[23]. Flagella are hollow helical tubes made of proteins that are attached to motor proteins imbedded in the cell membrane/envelope [24]. The helical structure introduces chirality and thus breaks symmetry, allowing for forward motion in low Reynolds number environments [19]. When these helical flagella are rotated counterclockwise (CCW), they form a bundle that propels the cell forward in straight (ignoring diffusion and morphological asymmetries) trajectories – often referred to as a 'run'. When the flagella are rotated clockwise (CW), they instead splay out and randomly reorient the cell – often referred to as a 'tumble' [25]. These types

of bacteria explore their environments primarily in a biased random walk via 'run-and-tumble' motion. In the absence of attractant or repellant chemical gradients, such bacteria perform an unbiased random walk by running for a random amount of time and then tumbling into a new direction of motion. In the presence of a chemical gradient cells alter the mean period between tumble events in response to changes in local chemical concentration thereby generating a biased random walk that ascends favorable gradients. . If a cell is going against the preferred gradient (down for attractants, up for repellants), it will decrease the mean run time and vice versa [14] increasing the probability of travel in the preferred direction.

Many bacterial environments – like soils or a mammalian gut – are structurally complex, wherein exploration of their environment requires interaction with objects and surfaces of varying shape, size, and curvature. Even in bulk fluid environments like the ocean, cells encounter, and are often chemotactically attracted to, particles that range in size from single to hundreds of microns [13], [26]. Recent work showed that in order to maintain efficient chemotactic motion *E. coli* actively decrease their tumbling rates when moving through environments that contain obstacles [27]. *Rashid et al.* showed that in a rectangular grid of circular and square obstacles, bacteria were able to maintain similar rates of chemotaxis regardless of the density or size of obstacles. However, in that work, no distinction was drawn between flagellar tumbling and changes in trajectory due to interactions with obstacles, thus the mechanism(s) by which cells maintain efficient chemotaxis in structurally complex environments remains unclear.

1.3 Bacterial Hydrodynamics

Bacteria propel themselves forward by creating a toroidal flow field around the cell body via flagellar rotation [28]. The CCW rotation of flagella produces a flow field that is well approximated by the field produced by a force dipole made up of two opposite force monopoles [28]. The monopole used is referred to as a 'Stokeslet', that is a Green's function solution of Stokes flow (fluid flow where inertial forces are negligible) [29]. By tracking small passive fluorescent tracers, this hydrodynamic model has been shown to be accurate up to tens of microns away from the cell body, except in the immediate side and rear of the cell where the force dipole model significantly overestimates the magnitude of flow [28]. This study also showed that when cells are within a few microns of each other, or of steric boundaries, hydrodynamic forces and Brownian angular diffusion likely dominate motion, but 'long-range' (>4 um) hydrodynamics have negligible effects on cell motion. From this starting point, current models of bacterial interaction with surfaces assume that viscous hydrodynamic forces alone describe deviations to cell orientation, and thus the direction of motion [30]–[32]. Steric interactions with surfaces are treated as a hard-core repulsion that acts to keep the cell body from overlapping with an object [31]. These models reproduce the deviations to trajectories produced by cell-surface interactions for large (low convex curvature) surfaces such as planes and large spheres and pillars ($R >$ 20 μm). When close to a planar surface (< 0.5μm), viscous forces, arising from the cellular flow field coupling with the surface (a no-slip boundary), create a force perpendicular to the direction of motion. This causes cells to swim in approximately circular trajectories that are restricted to motion along the 2D surface for tens to hundreds of seconds [16]. Similarly, bacteria are attracted to large circular pillars with sufficiently low (convex)

curvature where the pillar surface is assumed to be flat when considering hydrodynamic coupling [30]. This attraction maintains motion around the curved surface via torque on the cell body and flagellar bundle that orients the cell toward the pillar surface at a small contact angle [30]. [check what I said here] Finally, experiments show that attractive interactions cause rod-shaped Janus particle microswimmers to swim around spheres of sufficient size [33]; a mechanism underlying this effect was reported using the method of images to explicitly calculate the hydrodynamic coupling between cells and spheres [31], [32]. These models used different methods and assumptions, but both predict cell capture around a sphere whose radius is above a critical value. For spherical radii smaller than the critical radius the models predict the angular deviation to cell trajectories as they 'scatter' from the sphere. An early model proposed by *Spagnolie et al*. [31] gives extreme non-physical results as the sphere radius approaches the cell length. A recent model by *Zhang et al.* [32] attempts to rectify those issues by removing the assumptions of constant force and velocity. However, this model's predictions for small-obstacle interactions have yet to be experimentally tested. One study showed that the majority of interactions between cells and 3 μm diameter spheres led to 'forward scattering', defined as interactions for which the magnitude of the scattering angle was less than $\pi/4$ [34]. This appears to disagree with the model proposed by *Zhang et al.*, which predicts that for such small obstacles most interactions should result in scattering angles greater than $\pi/4$, but the experimental data lack the resolution to perform a quantitative comparison. Interactions with such small obstacles are biologically relevant, as wet soil types contain a majority of particles (by number) with radii less than 30 μm [35], [36]. In order to better understand the physical mechanisms that underlie interactions between swimming cells and small obstacles, we

studied bacterial collisions with small circular pillars, which I discuss further in Chapter IV.

1.4 Collective Motion

Collective behavior is seen across many scales in active-matter systems ranging from flocking starlings [37], [38], ants [39], schooling fish [40], locusts [41], and bacterial suspensions [42]–[45]. High density populations of bacteria are an ideal model system for the study of collective motion. A wide variety of genetic and chemical tools are readily available to manipulate cell phenotypes including morphology, motility, and chemotactic response, among others. Also, their high reproductive rate and small size allow for high-throughput experimentation, especially when compared to macro-organisms (i.e. schooling fish, flocks of birds). As cell density increases, hydrodynamic and steric interactions between neighboring cells become more frequent, to the point that a cell trajectory can only be described in the context of the collective motion of the population. The swarming motility of *B. Subtilis* colonies on sufficiently wet surfaces exemplifies this type of motion. Classically, swarming motility is defined by high-speed multicellular movement of bacteria propelled by flagella across a surface [45]. When swarming, cells up-regulate flagella number [18] and by secreting a surfactant draw fluid from the surface which allows individual cell motion and creates surfactant gradients that drive colony expansion through Marangoni flows [46]–[50]. Individual cells within a high-density swarm cannot move in the 'normal' run-and-tumble way as their motion is dominated by 'turbulent' interactions with other cells [51]. By observing a subpopulation of fluorescent cells imbedded within a larger population of non-fluorescent, but otherwise identical cells *Ariel et al.* were able to collect high resolution trajectory data of individual cells in swarms. They showed that

individuals migrate around the population in a Lévy walk [52]. A Lévy walk is a random walk where actors move with a fixed speed making sharp reorientations at random times, where the period between reorientations is drawn from a power-law distribution [53]. Swarming dynamics can also impact the diffusive properties with an environment. For instance, *Be'er and Harshey* observed the upper super-diffusive dynamics in the fluid-air boundary of a fluid layer containing swarming bacteria [54]. Swarming motility is a common phase of bacterial collective motion [55], but models have postulated the existence of other motile phases. By modeling bacteria as self-propelled steric rods moving in two dimensions, *Wensink et al.* proposed the existence of multiple phases of bacterial motion (or non-motion) as a function of cell density and cell-body aspect ratio [51]. *Be'er et al.* showed that increasing cell aspect ratio (making cells longer while keeping cell diameter constant) above a threshold value shifts the phase of collective motion. At low aspect ratios, the cell density distributions are unimodal, indicative of being in the swarming state. At high aspect ratios, the cell density distributions are a superposition the low-density and high-density population [55]. Both of these studies also suggest that at sufficiently high cell densities a jammed phase should emerge in which cellular motion ceases due to confinement by neighboring cells. While this phase was not explicitly shown in their experiments [51], [55], work in the Ursell Lab (on which I was an author) [50] provided strong evidence for the existence of such jammed states, as well as active transitions between jammed and collectively motile phases. In the unimodal density swarming state, *Be'er et al.* observed statistics of motion that were insensitive to changes in cell density (up to a limit) and insensitive to relatively small perturbations in the aspect

ratio. This suggests that swarming motility is a robust mode of collective motility that plays an important role in the natural motion and spread of bacterial colonies on surfaces.

Previous experiments primarily used isogenic and isophenic cell populations to better understand how specific parameters like cell density, environmental geometry, and cell morphology govern group motility [48], [50], [55], [56]. However in natural systems, cellular heterogeneities in morphology, phenotype, and even species are the norm [57], [58]. While small changes in cell aspect ratios do not seem affect swarming motility, it remains unclear how the composition of motile phenotypes within a collective affect collective motion and behaviors. We explore this by studying the motility of mixed populations of motile and non-motile *B. subtilis* in Chapter II. Some of the work described in this dissertation is based on co-authored material, especially Chapter IV which, at the time of writing, was recently submitted for peer review.

CHAPTER II

COLLECTIVE MOTION IN BACTERIAL POPULATIONS WITH MIXED MOTILITY GENOTYPES

2.1 Collective Motion of Bacteria

The motion of large, densely packed groups of organisms is often qualitatively distinct from the motion of individuals, yet hinges on individual properties and behaviors. Such collective behaviors are seen across many scales in active-matter systems from starling flocks [37], [38] to ants [39], [59], [60], and to bacterial suspensions [42], [61], [62]. High density populations of bacteria are an ideal model system for the study of collective motion for numerous reasons: (i) their high reproduction rate and numbers enable high-throughput experimentation, (ii) their size allows for low-cost fabrication of physically and chemically controlled environments in which to observe their motion, and (iii) it is possible to genetically modify bacteria to vary both morphological and phenotypic cell properties. At sufficiently high densities, the motion of individual cells is perturbed by interactions with other cells such that their trajectories are often better described by the bulk motion of the collective. The collective motion of bacteria (of which there are many kinds) has been observed in different environments such as hard surfaces [52], [63], bulk suspensions [64], [65], thin fluid suspensions [50], [66], and artificial devices in a variety of geometries [67]–[69]. These studies observed strong effects between the physical environment (especially confinement) and the bulk motility of swarming cell populations.

Many of these studies were conducted using rod-like cells in the 'swarming' state of collective motion, which is characterized in open environments by dense cellular packings with high-velocity turbulent bacterial flow [51]. However, other states of collective motion have been predicted by modeling and observed experimentally as a function of cell density and the aspect ratio of rod-like cell bodies. Using a self-propelled rod (SPR) model, *Wensink et al.* proposed the existence of six states of collective motion ranging from the low-density 'dilute' state where swimmers act independently; the medium density 'swarming' state characterized by large spatial and temporal density fluctuations; the high aspect-ratio 'laning' phase where cells achieve global alignment (i.e. high nematic order); the 'bio-nematic' phase where vortices and jet structures coexist; the 'turbulent' phase characterized by chaotic motion and velocity correlations on the order of ~$5\mu m$; to the 'jammed' state in which low aspect-ratio cells are so tightly packed (i.e. high packing fraction) that they cannot move [51]. Some of these states have been shown to exist experimentally by adjusting the aspect ratio of cells and their overall density. *Be'er et al.* showed that increasing the cell aspect ratio above a critical value shifted cells from a swarming, turbulent state to two different states depending on cell density. At low density, they observed a state characterized by small clusters of these long cells moving together while at high density, they observed these clusters grew to the size of the viewing frame. These states are reminiscent of the 'swarming' and 'laning' phases predicted by the SPR model [55]. These studies highlight the control that cell density and morphology have over the collective behaviors of high-density cell populations.

Previous experiments primarily (and reasonably) used isogenic and isophenic cell populations to better understand how specific parameters – like environmental geometry,

cell density, and morphology – influence collective behavior [48], [50], [55], [56]. However, in natural systems, multiple distinct cellular phenotypes (of the same species) are often found coexisting within bacterial populations [57], [58]. Thus we hypothesized that the phenotypic ratio of a bacterial population would also be a distinct parameter that affects collective motility and might produce additional, distinct phases of motion. To characterize how different motility phenotypes affect each other and group motility, we imaged the collective dynamics of wild-type *Bacillus subtilis* with varied concentrations of a non-motile mutant doped into the population. In these mixed motility-phenotype populations, we observed a transition from turbulent behavior to highly constrained semi-ballistic motion as the fraction of non-motile cells increased – we call this new phase 'ant trailing', for reasons that will become clear below. We also observed an exponential decay in the mean speed of the group as the fraction of non-motile cells increased. This work illuminates the role that individual cell behaviors play in the emergence of collective motion. It also suggests that phenotypic mixture within a population may shift material transport properties into qualitatively distinct regimes.

2.2 Methods

These experiments used (i) wild-type (WT) *Bacillus subtilis* (3610 parent strain) labeled with cytoplasmic GFP DK1203 and (ii) DS1677 Δhag, a non-flagellated mutant strain (from 3610 parent strain) with a genomic deletion that abolishes filament assembly – hence the cells are (nearly) metabolically wild-type, but are immotile. Agar plates containing Terrific broth (TB) (Sigma Aldrich) and 100 $\mu g/mL$ spectinomycin (for the GFP labeled cells), or simply TB and agar (for the unlabeled Δhag cells) were streaked from frozen stocks to produce single colonies. Prior to experiments, GFP labeled cells were

picked from single colonies taken from the agar plates, and grown in TB with 100 $\mu g/mL$ spectinomycin for six hours, shaken at 37℃. The unlabeled and unflagellated (non-motile) mutant divides at a higher rate, thus the two cultures were density matched prior to mixing by measuring optical density (OD620) with a NanoDrop 2000 Spectrophotometer. We then mixed each of the matched cultures at a known ratio to create 1 ml of mixed-motility culture – two independent variables were controlled at this point: (i) the overall number density of all cells in solution and (ii) the ratio of motile to non-motile genotypes. This suspension was then pelleted in a centrifuge at 1000g for three minutes and resuspended in 50 μL of TB to increase overall cell density. From this high density suspension a 5 μL droplet was deposited onto a small (~19 mm diameter??) circular Luria broth (LB) agar pad. The pad was cast in a silicone isolator (Grace Bio-labs), and allowed to cool and solidify at RT for three minutes. A thin #1 coverslip was laid over top, and sealed against the silicone, forming a closed viewing chamber. This created a thin (1.5 – 2 μm) fluid environment where we observed large regions containing cells that were constrained to quasi-2D motion in a single monolayer of cells. We imaged cell motion in phase-contrast with an automated Nikon Eclipse TI-E fluorescence microscope using a 40x CFI Plan Fluor DLL Ph2 objective with an optional 1.5x multiplier tube. Images were collected with an Andor iXon EMCCD camera. When capturing images using the full resolution of the CCD, the maximum capture frame rate was 21.45 frames per second. When motile cell fraction (and hence mean cell speed) was high, we increased the frame rate of image acquisition by using a smaller region of interest (ROI) on the CCD, which increases maximum framerate by decreasing the read-time. Due to an unknown (and we believe still uncharacterized) reaction, *B. subtilis* cells reacted to GFP illumination light (blue light) by ceasing motility

within seconds, thus we imaged all motion in phase contrast. Due to randomness in the mixture and the inherent difference in motility between the two genotypes, the ratio of motile to non-motile cells between viewing frames was often different from the overall mixture ratio. To measure the local ratio of genotypes we first captured a fast (>20 fps) image series over the course of minutes using phase-contrast to measure motility; we then captured a single GFP image of the tagged motile DK1203 *B. subtilis* to measure the local concentration of motile cells.

At the highest cell-number densities, and owing in part to the high auto-fluorescence of LB agar, individual cell identification required to measure collective motion in phase-contrast and GFP fluorescence was difficult and unreliable. Therefore, in order to measure genotype concentrations we instead counted pixels. First, we examined the phase contrast images and defined a threshold below which pixels were defined as cell pixels, brighter pixels were considered background pixels – this defined the fraction of pixels (ρ_1) that corresponded to a cell of either genotype. Second, we captured a single GFP image and measured the fraction of pixels (ρ_2) whose intensities were above a threshold. That threshold corresponded to segmentation of contiguous pixels groups whose size and shape approximately matched the known dimensions of the fluorescent cells. Thus, the number-density of cells is proportional to ρ_1 and the ratio of motile / immotile cells is $\rho_2/(\rho_1 - \rho_2)$. To identify pixels in phase-contrast images that belonged to cells we used a thresholding algorithm. We smoothed the image with a 3 x 3 pixel median filter, then fit the distribution of pixel intensities to a double-Gaussian distribution with one Gaussian corresponding to the (brighter) background pixels and the other to the (darker) cell pixels. In phase-contrast cells appear darker than the background, thus the threshold was set by

calculating the mean of the cell-intensity distribution and adding two standard deviations – pixels above this limit were considered background. For GFP images, we applied the extra step of removing low frequency noise (the illumination profile) by subtracting from the original image a copy whose intensities were filtered with a 300-pixel radius Gaussian convolution. The threshold was set at two standard deviations above the mean of the background. The resulting binary images were visually inspected, and found to be consistently accurate for the phase-contrast images. Due to high auto-fluorescence in the media and differences in cell brightness, the GFP images were of variable quality, accuracy of the thresholding method has an unknown but nontrivial uncertainty. We used Particle Image Velocimetry (PIV) (specifically the PIVlab MATLAB tool [70], [71]) to measure collective motility in these 2D cell monolayers. This resulted in spatial maps of time-dependent velocity vectors associated with bulk cell motion. PIV algorithms generally work by excising small portions (e.g. 32 x 32 pixels) of the image, then computing the correlation matrix of that interrogation area within a zone of nearby pixels in neighboring frames across time, thus allowing calculation of a displacement vector. To increase computational speed, PIVlab performs a discrete Fourier transform on the image in order to compute the correlation matrix in frequency space [71]. With PIV, we measured the velocity at points with spacing 2.6 μm in a grid across our image. Velocity values from grid points on the image edge were ignored.

In the following sections we limit our analysis to 14 individual image stacks in which cell-number density was constrained to $0.6 \leq \rho_1 \leq 0.7$.

2.3 Results

To understand the effects that non-motile cells have on swarming bacterial populations, we measured the local cell velocities of high-density mixed-motility populations within a narrow window of cell density. First, we looked at the mean speed $\langle|v|\rangle$ of these collectives as a function of the fraction of non-motile cells within the population, Φ. A naïve hypothesis was that this value would scale linearly, from the mean speed of swarming WT *B. Subtilis*, to zero (or some small value corresponding to the noise floor) when the entire population was non-motile. Such a hypothesis ignores interactions between motile and non-motile cells, and assumes that the mean speed is proportional to the total force applied by cells within the population. This is a reasonable (naïve) assumption because in low Reynolds-number contexts, like this, the velocity of an object is proportional to the applied force. Therefore, if the force for motion is generated by a subpopulation of cells and is then 'shared' by all cells (motile and non-motile) the mean speed of the population would be proportional to the mean force per cell

$$F_{Tot} = N_{WT}F_{WT} = (1-\Phi)F_{WT} \tag{1}$$

$$F_{Avg} = \frac{N_{WT}}{N_{Tot}}F_{WT} = (1-\Phi)F_{WT} \tag{1}$$

where F_{WT} is the force applied by a single wild-type cell. Swarming motility is characterized by nearly constant cell-cell interactions [51], and observations by eye of all our collected images clearly showed cells sterically (among other mechanisms) interacting with each other. When a single motile cell collides with a single non-motile cell, we saw the motile cell's velocity decrease, owing to either a portion of the propulsion force pushing the non-motile cell or the motile cell being unable to push a larger mass of non-motile cells

and thus temporarily halting. However, instead of a simple linear relation between $\langle|v|\rangle$ and Φ we found that the data was approximately described the exponential function

$$\langle|v|\rangle = v_o e^{-\Phi/\Phi_o}$$

with $v_o = 27\ \mu m/s$ being the mean collective swarming speed when all cells are motile, and $\Phi_o = 0.23$ being the characteristic density of non-motile cells that results in significant slowing of group motility (Fig. 2.1). We found these parameters by performing a linear fit to the natural logarithm of the mean speed versus the fraction of non-motile cells. These data (fig. 2.1) do not match the linear prediction above, rather they hint at more complex interactions between motile and non-motile genotypes.

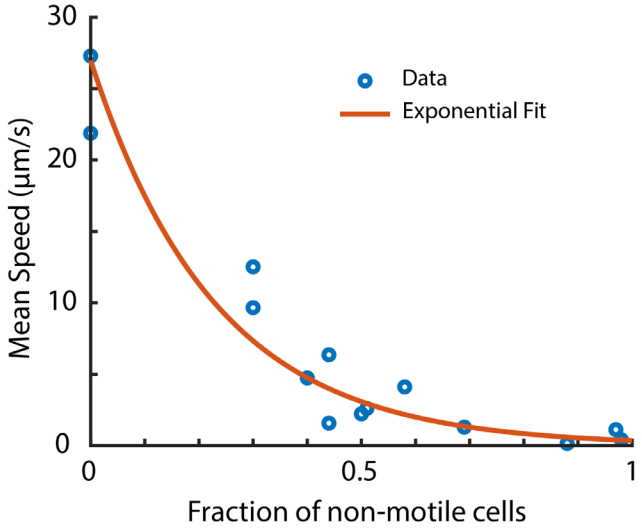

Figure 2.1: Plot of the time-averaged speeds of bulk cell populations versus the fraction of motile cells present, across 14 imaging data sets. The exponential fit has a decay constant of $\Phi_o = 0.23$ and maximum speed $v_o = 27\ \mu m/s$. Mean speeds in a square grid with vertices 2.6 μm apart were acquired with Particle Image Velocimetry (PIV) using the MATLAB PIVlab tool [70]. The fraction of motile cells was determined by calculating the number of pixels belonging to cells via thresholding the phase-contrast images, then calculating the number of pixels belonging to motile cells via thresholding the GFP images. There are significant but unknown errors in the values these fractions and thus error bars were omitted.

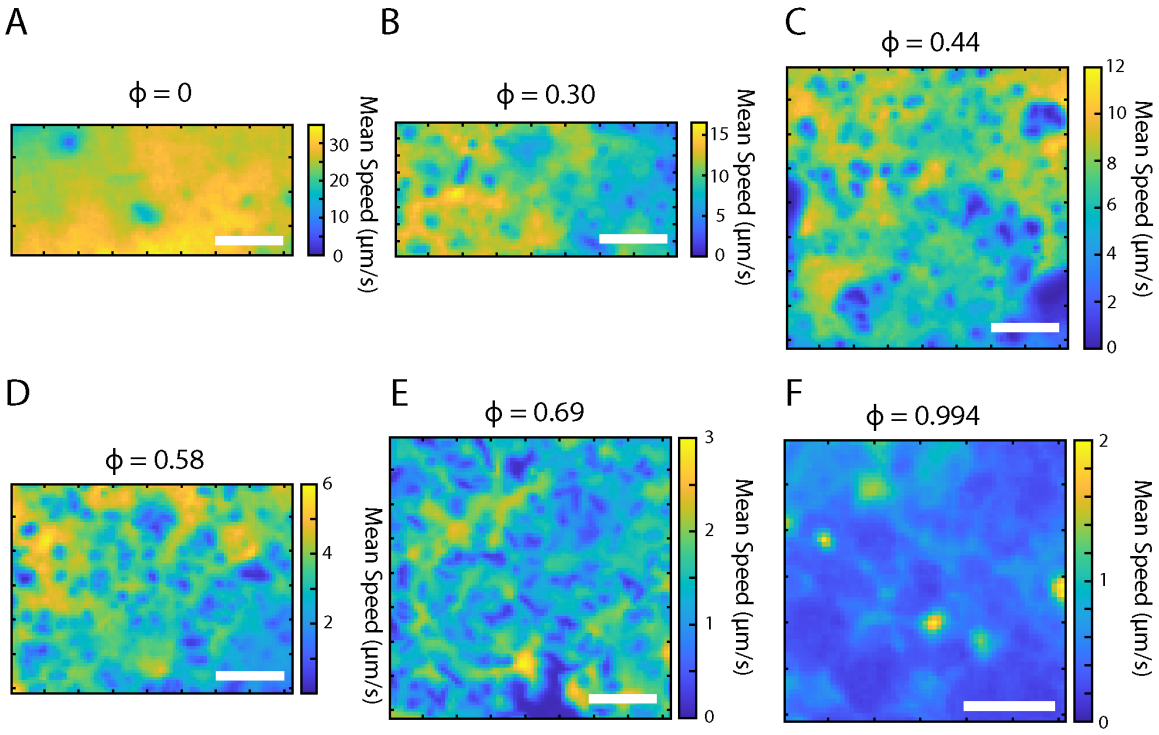

Figure 2.2: Heat maps of the spatial distributions of mean speeds from PIV velocity vectors found from data sets at six different values of non-motile cell fraction Φ as labeled. The scale bars are 50 μm. The variation in image size reflects the different ROI's required to capture data at higher frame rates. The mean speed decreases as Φ increases, clearly seen from the individual heat maps, which are plotted at different scales to highlight spatial structure of the velocity field. Across all densities, there were clear divisions between areas of low mean velocity (darker areas) and areas of high mean velocity (brighter areas). Within areas of low mean velocity, we observed clusters of non-motile cells surrounded by motile cells that are sterically forced to move around these stationary clusters.

We also saw distinct changes in the trajectories of the WT cells as we increased the fraction of non-motile cells present within the population. As the fraction of non-motile cells increased, we saw larger and more frequent areas of low mean velocity (Fig. 2.2). These areas, while largely composed of nonmotile cells, also appear to contain some motile cells that become stuck in the larger mass of nonmotile cells. Thus, we see a clear spatial

pattern of high and low motion which persists across time (i.e. in the time-averaged velocity magnitudes) (Fig. 2.2). Once Φ rose above ~0.9, a new kind of collective motility emerged. Motile cells repositioned non-motile cells to carve paths that were then subsequently reinforced by other motile cells traversing those same (or very similar) paths, producing the 'web' pattern of higher mean speeds seen in figure 2.2 F. Frequently, when motile cells collided with non-motile cells, non-motile cells are forced apart creating a way forward and simultaneously leaving an open path where they passed. These paths persisted for seconds and frequently had multiple motile cells pass through them, as such routes offer the path of least resistance to motion. These subsequent motile cells reinforce the paths (i.e. keep them open) until, after ~5 – 10s, the persistent paths were closed by the bulk movement of non-motile cells created by other motile cells creating new paths through the bulk of non-motile cells in another location (Fig. 2.3). Motion in these paths appears to be semi-ballistic in nature as the paths themselves are seen to be relatively straight segments of open space. This is in stark contrast to the highly turbulent motion observed in the low Φ swarms as seen by us and previously described in (e.g.) [52], [55], [72].

2.4 Conclusion and Discussion

We explored a previously unstudied aspect of active matter: the mixing of motile and nonmotile agents. To do this we analyzed the spatial velocity fields of dense *Bacillus subtilis* populations across a range of relative concentrations of motile and non-motile cells. We found evidence for an exponential relation between the mean population speed and the fraction of motile cells in high density cell populations.

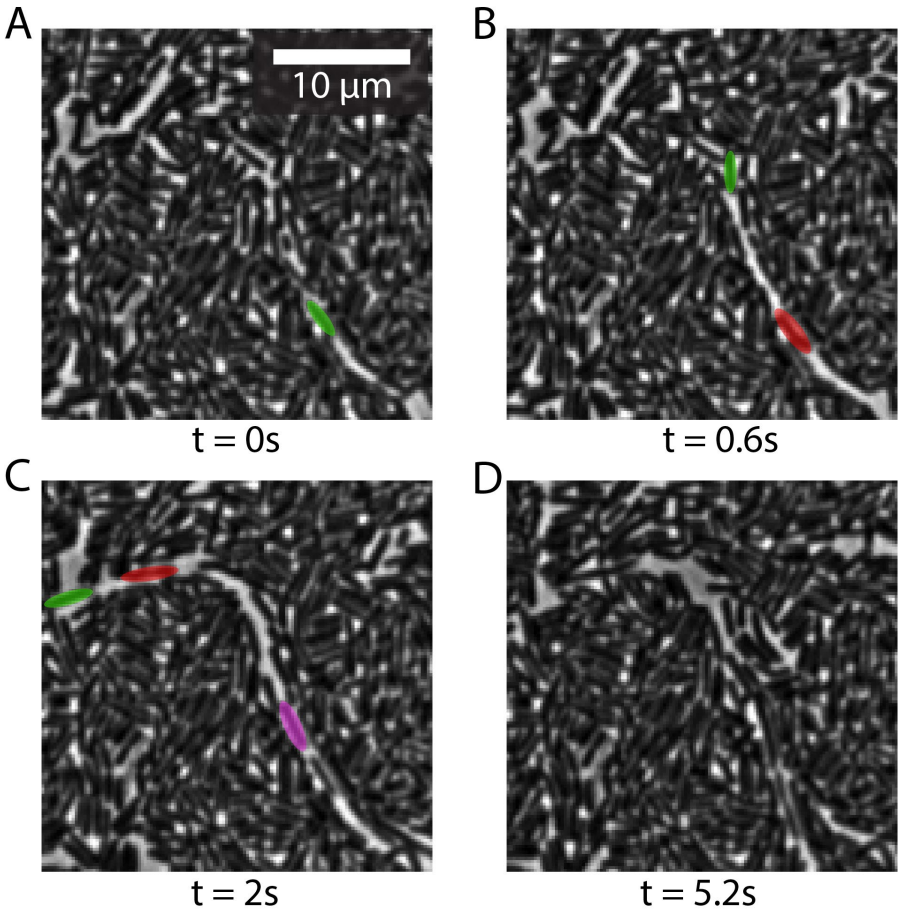

Figure 2.3: A time-lapse of path creation, persistence, and destruction in high a Φ population. (A) The first cell (green) encounters a mass of nonmotile cells. (B) The green cell forces its way through them creating an open path behind it. It is then followed by the second cell (red). (C) The first and second cells (green and red) continue to the edge of the frame while more cells (magenta) follow the persistent open path. (D) After 5 seconds, the path has been (mostly) closed due to random motions of the non-motile cells caused by other motile cells.

We also observed what appears to be a smooth transition between turbulent swarming motility and highly constrained semi-ballistic motion in these mixed populations as the fraction of motile cells decreased toward zero. While these measurements were made with *B. Subtilis*, the physical context that results in these observations may make these findings

applicable to not only other microorganisms but generally to active-matter systems of 'swimming' rod-like particles with mixed motility behaviors.

This work was limited in its scope due to difficulties inherent in the experimental setup. First, due to the inherent difference in motility between the two sub-populations, there was very little control over the fraction of motile cells in a given observation window. This forced us to estimate motile fraction by eye during an experiment, and then quantitatively measure the fraction *post facto* by analyzing the brightfield and GFP images as described previously. As a consequence, data acquisition across Φ was not systematic. Second, we had a similar lack of control over the number-density of cells, and again could only rely on rough estimates during experiments to guide data acquisition. Thus, number-density was also measured *post facto*, resulting in our data spanning a range of density ($0.4 \leq \rho_1 \leq 0.8$). However, cell density has strong effects on fundamental aspects of collective motion, like mean cell speed and mean-squared displacement [55]. Therefore, to isolate the effects of motile cell fraction on collective motion, it was necessary to maintain a nearly constant number-density while comparing variations in Φ – this restricted our analysis to a subset of our acquired data. Third, to create our quasi-two dimensional environment we used an agar pad cast in a silicone isolator and sealed with a glass slide. This created an environment of non-uniform height, as agar surfaces have nontrivial roughness. Thus areas of the device that where the height was between 1.5 and 2 um (and hence motion was quasi-2D) were limited. Lastly, due to the high auto-fluorescence of rich media, our fluorescence images of GFP-labeled motile cells were of variable quality leading to unknown but nontrivial uncertainty in our measure for Φ. These experimental uncertainties spurred us to develop microfluidic devices within which we could exert

superior control over these key variables. This led to our development of a novel method for the creation of microfluidic devices (chapter III) and led to our experiments on cell-obstacle interactions (chapters IV and V). However, despite these difficulties, we observed previously unseen behaviors in bacterial motion and evidence for exponential scaling of mean speed with respect to the fraction of non-motile agents in an active matter system.

CHAPTER III

FABRICATION AND DESIGN OF MICROFLUIDIC DEVICES

3.1 Introduction

To overcome many of the problems we encountered in our previous experiments outlined in Chapter 2, we began designing and fabricating microfluidic devices using photolithography. Microfabrication of microfluidic devices allows for the creation of highly controlled environments in which to live-image microorganisms. For example, one can create chambers of arbitrary and unique shapes within which bacteria explore and interact [61], [68], [73], [74]. They allow for the fabrication of steric objects such as posts of various shapes [27], [30], [75] and moveable objects such as spheres or even micron-scale gears [34], [76]. Pumps control fluid pressure across the device with high precision to test the effects of fluid flow on bacterial motion [77]–[79] and colonization of surfaces [74], [80], [81]. Chemical gradients across the device can be created to precisely test the chemotactic response in motile bacteria [82]–[84]. The confinement and isolation of fluids loaded into microfluidic devices also allows for precise control over cell density. When studying the dynamics of single-cell behavior, it is important have low enough cell density to keep cell-cell interactions at a minimum while maximizing the number of observed cells to efficiently collect data. On the other hand, when observing higher density swarms and how cell-cell interactions affect the dynamics of collective motion, precise control of cell density can help eliminate a major source of noise in data collection. Frustrations over the

lack of control over cell density when conducting the phenotypic mixing experiment (chapter 2) led to a renewed effort to design microfluidic devices to observe cells. The ability to fabricate small steric obstacles down to length scales of a single cell length enabled our cell-pillar scattering research outlined in Chapter 4. This chapter first outlines classic soft lithography techniques for fabricating microfluidic devices, and the disadvantages and limitations these devices have, which led us to develop a novel technique for microfluidic device fabrication. The chapter then gives a detailed description of our novel fabrication technique and explores the advantages and disadvantages of these devices.

3.2 Soft Lithography

Typically, microfluidic devices are made using a technique generally referred to as 'soft lithography' [85]. The general makeup of these devices is molded Polydimethylsiloxane (PDMS), bonded to a glass substrate. PDMS is a silicon-based organic polymer which has a few key traits that make it ideal for soft lithography. Before curing, PDMS is viscoelastic and will conform to the surface that it is poured onto over a large area with sub-micron precision [85] and after it has been cured, its elasticity allows for relatively easy release from the molding substrate. Second, it is chemically inert which ensures that cells' only interaction with the surface is mechanical. Third, it is optically transparent which makes it ideal for imaging with both bright-field (including phase-contrast) and fluorescence microscopy. Fourth, the materials involved are cheap and fabrication can be completed in hours which allows for iterative prototyping. However, these devices are difficult to clean well and, in many contexts, are single use devices which makes the low cost essential. Last, it can be UV or plasma oxidized to alter the surface chemistry to allow for chemical

bonding to glass substrates [86]. When purchased, PDMS typically comes in two parts, the elastomer base, and the elastomer curing agent. For normal use, these are mixed 10:1 base to curing agent by weight and increasing the amount of curing agent can increase the post-cured PDMS stiffness [87]. This tunable stiffness, and the relatively low stiffness of PDMS overall, is an essential component of more complex microfluidic devices which use multiple layers to create valves and pumps within the device itself [88]. Once the two parts are mixed together and heated to 100 °C, the curing agent will crosslink the polymer into its hardened form within an hour.

To create the molded PDMS, first the negative of the desired final pattern was fabricated on a silicon wafer using photolithography (photolithography described in detail in section 3.3) to create a 'master mold'. This master mold must be treated with trichlorosilane to make the surface hydrophilic and thus reduce adhesion between it and the hydrophobic PDMS. Once the master mold was treated, new, uncured and well-mixed PDMS was poured onto the mold. To increase optical clarity, it is important to degas the PDMS in a vacuum chamber to remove microscopic air bubbles which can disrupt the light path. The degassed PDMS was then placed in an oven to crosslink for an hour, left to cool, and carefully removed from the master mold. Next, to bond the molded PDMS to a glass substrate (often a microscope slide) the PDMS and glass surfaces were activated using a UV-Ozone oven with no heat for 1 hour. Once activated, the surfaces were mechanically compressed by resting a small weight (~100g) on them and heated on a hot plate for 30 minutes at 90 °C. Once bonded, the device can withstand some positive pressure, but over-application can cause leaks in the device.

Soft lithography supports a limited range in the aspect ratio (height : width) of structures and gaps between structures in the device. We found that creating high aspect ratio structures, (greater than 5:1) especially when those structures are small (<5 μm radius) becomes difficult and unreliable. First, removal of the structure from the mold became unreliable as many of these structures were stuck in the mold and torn from the bulk PDMS device. Second, high aspect-ratio structures (like our smallest pillars) tended to bend or collapse before they could be bonded to the glass substrate causing deformations in the desired structure of the device, frequently rendering whole regions useless. On the other hand, the aspect ratio of space between structures has a minimum threshold. We saw that when the gaps between structures are more than ten times the device height, there was a high risk of device collapse due to the low stiffness of PDMS. This is especially problematic when negative pressure was applied to flow media through the device (which is the norm to maintain the bonded seal). In our research observing bacterial interactions with small, high-curvature steric objects (Chapter 4) we required structures with a radius less than or equal to 5 μm with a small device depth (<20 μm) to be able to capture the entire *z*-depth when imaging. We also required the device depth to be a minimum height in order to keep hydrodynamic resistance low enough to flow media through the device . When device height falls below 10 um (?) flow resistance and internal surface tension effects prevent full-device flow.

The hydrodynamics of microfluidics is well described as an analogy to electrical circuits. Fluid flow replaces electric current, the applied pressure replaces voltage, and the hydrodynamic resistance due to the geometry of the flow channels and fluid viscosity

replaces electrical resistance. In a rectangular channel whose height is less than the width, hydrodynamic resistance is well approximated as

$$R_h \approx \frac{12\mu L}{wh^3\left(1 - 0.63\frac{h}{w}\right)}$$

where R_h is the hydrodynamic resistance, μ is the fluidic viscosity, L is the channel length, w is the device width, and h is the device height [89].Thus, the resistance of devices with typical dimensions (w = 0.1 *mm*, L = 1 *mm*) and small heights ($h \leq 5\ \mu m$) is such that to create a modest flow rate of 10 *nL/s*, the pressure required becomes greater than 1 *atm* and is therefore impossible with application of negative pressure (and positive pressure above ~ 1 *atm* unseals the device). In order to maintain low resistance and remain within the depth-of-field of our Plan Fluor ELWD 20x Ph1 ADM microscope objective we chose a 15 μm device height. Given this, we were still presented with two problems. First, with a 15 μm height, the maximum gap width between structures was 150 μm; this presented difficulties when collecting control data (in feature-less areas) of bacterial trajectories on the length scale of motion persistence . Second, our smallest features pushed the bounds of reliability in molded PDMS device creation. In our early designs, we had very low success rates with the creation of features with R < 5 μm.

To overcome these limits, we developed a novel method for the creation of microfluidic devices that involves creating device features directly onto a silicon or glass substrate using photolithography (Fig. 3.1). These devices were sealed with a thin (< 100 μm) layer of PDMS bonded to a glass slide which acts as a uniform, stiff gasket. With this technique, it was possible to create high aspect-ratio structures beyond the limits of typical PDMS construction, and the increased stiffness of thin PDMS bonded to glass allowed for

significantly larger (> 0.5 *mm*) featureless areas. This device relied on two separate unbonded pieces that remain sealed only when negative pressure was applied but was easily separated post-experiment and thoroughly cleaned for reuse (described in section 3.4). The structures made from photoresist have the 'feature' of being mildly auto-fluorescent, enabling detection of surface structures without significant degradation in signal-to-noise of cellular intensities. A key disadvantage with this method was that it was only capable of creating single layer microfluidic devices which prevented creating many of the complex and interesting components of microfluidic designs (i.e. valves and pumps).

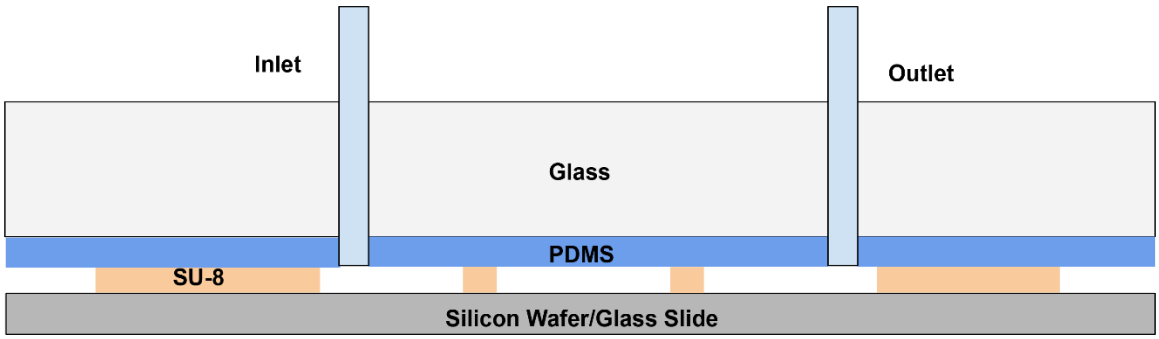

Figure 3.1: A simple schematic of our atypical microfluidic devices consisting of SU-8 photoresist directly patterned onto a Silicon wafer or glass substrate, then sealed by a PDMS gasket adhered to a glass top-piece. Direct patterning of SU-8 allows for higher spatial resolution and higher aspect-ratio structures. The thin layer of PDMS bonded to glass creates an airtight seal whose with high effective stiffness supports large open areas within the device without risk of collapse.

3.3 Novel Fabrication Method: Substrate and Features

To begin fabrication, the desired features of the microfluidic device (chambers with and without pillars, flow channels, etc.) were created directly in photoresist on a silicon or

glass substrate using standard photolithography. Generally, photolithography is the process of fabricating micro/nano structures using a light-activated polymer. Light is shined (either through a patterned mask or with a laser) onto the photoresist and then the exposed (if negative photoresist) or unexposed (if positive photoresist) resist is rinsed off the sample. Our devices used SU-8 2000 negative photoresist manufactured by Kayaku Advanced Materials. SU-8 photoresist is primarily Bisphenol A Novolac epoxy dissolved in an organic solvent and up to 10% (by weight) Triarylsulfonium/hexafluoroantimonate salt which acts as the photoacid. First, we covered the substrate with photoresist by spin coating a thin, defined, and largely uniform layer of photoresist onto the substrate. Spin coating is a process by which rotating the substrate with photoresist poured on creates different layer thickness based on the viscosity of the resist which is controlled by the ratio of epoxy to solvent. For thicker layer resists ($\geq 10\ \mu m$) there is often an over-thick ring of resist at the edge of the substrate (commonly referred to as an 'edge bead'), which we removed using a lint-free disposable wipes soaked in acetone. This ensured good contact with the patterned center of the substrate in later steps and in the final product. We first used SU-8 2000.5 to create a 0.5 μm base layer and patterned SU-8 2015 on top of the base layer to create our 15 μm tall features. The base layer was used to increase the resolution of pattered structures and to increase adhesion of small features onto the substrate (especially important on glass substrates). The base layer was made by simply using the manufacturers guide to fabrication – the photoresist iss spun-coat at 3000 RPM for 30 seconds, soft baked at 95 °C for one minute, exposed for a total dose of 60 mJ/cm^2, post-exposure baked (PEB) for 1 minute at 95 °C, and then hard baked for 10 minutes at 200 °C (these steps are described in greater detail below). The SU-8 2015 was also deposited by spin coating at

3000 RPM for 30 seconds with the edge bead manually removed. Next, the sample was 'soft baked' for five minutes at 95 °C on a hot plate to evaporate solvent and harden the photoresist to ensure that it kept its shape and did not stick to the photomask. If the substrate was thick (such as a glass microscope slide) soft bake times were increased to ensure that the photoresist reaches temperature. The soft bake can create stress on the photoresist causing wrinkling and other deformities, and in thick ($> 50\ \mu m$) layers of resist, the solvents may evaporate quickly from the top trapping solvent in the lower layer causing z-axis asymmetry in features. In this event, the temperature must be ramped from 65 to 95°C over the course of several minutes. Next, the photoresist was exposed to ultraviolet light with a SUSS MicroTec MJB4 mask aligner which uses an Hg lamp as its UV source to initiate crosslinking of the polymer. A mask aligner has two main components, the UV light source with associated optics, and the sample stage underneath the photomask mount. For a negative resist like SU-8, the photomask is the negative image of the desired pattern of developed resist. UV photons which pass through the mask react with the salt to create hexafluoroantimonic acid which protonates the epoxide groups in the resin monomers [90] which is the first step in the crosslinking that hardens the SU-8 leaving the desired features after development.

When exposing the photoresist, it was necessary to filter-out wavelengths of UV light below 360 *nm* to avoid a common deformation known as 'T-topping', which is characterized by a larger, overdeveloped top-layer on features (fig. 3.2). SU-8 has high absorbance of high-frequency ultraviolet light which causes the top few microns of exposed SU-8 to absorb nearly all of the high-frequency light, leaving the lower section to absorb UV wavelengths greater than 360 *nm*.

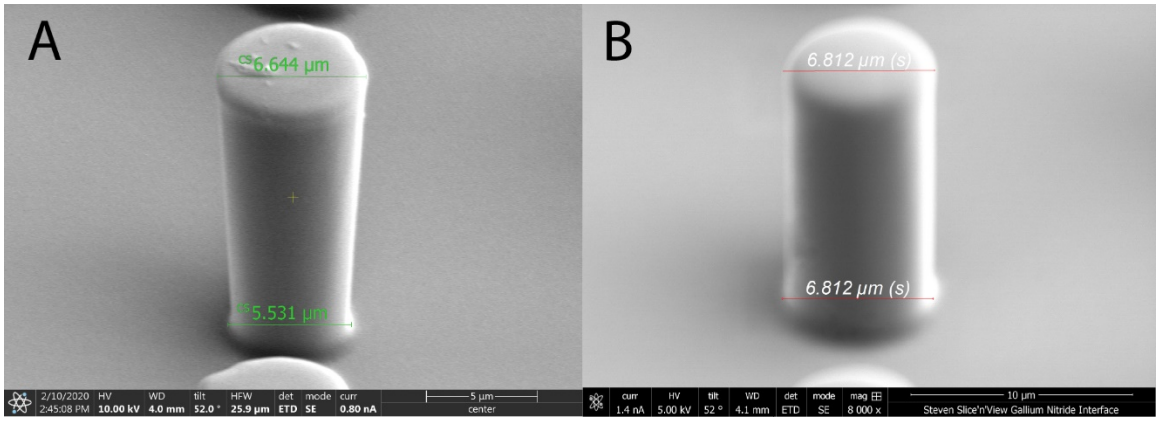

Figure 3.2: EM images of fabricated pillars. (A) 15µm tall SU-8 pillar showing T-topping exposed using a Hg lamp without a filter. The T-topping is characterized by the overexposed and thus oversized top of the structure. For the pillar shown, the base is ~5.5µm in diameter while the top is ~6.6µm in diameter. (B) 15µm tall SU-8 pillar made with a Hg lamp through a Hoya L-37 long-pass filter. Note the vertical sidewalls and uniform diameter across *Z*.

The high-frequency UV naturally carries more energy which causes the top layer to become significantly overdeveloped and creates an overabundance of acid in the top layer. The acid diffuses outward, leading to poor resolution and increased size on the top few microns while the rest of the feature resolves as designed. To fix this problem, we put a Hoya L-37 long-pass filter in the exposure light-path directly over the mask. In order to create our smallest features (R < 10 μm) and to achieve straight, symmetric features in general, it was necessary to increase exposure of the resist, beyond the manufacturer-provided dosage, to 240 mJ/cm^2 on the silicon substrate (Fig. 3.3). To expose the resist in our desired pattern and achieve appropriate resolution in our smallest features we used chromium photomasks (described in detail in section 3.5).

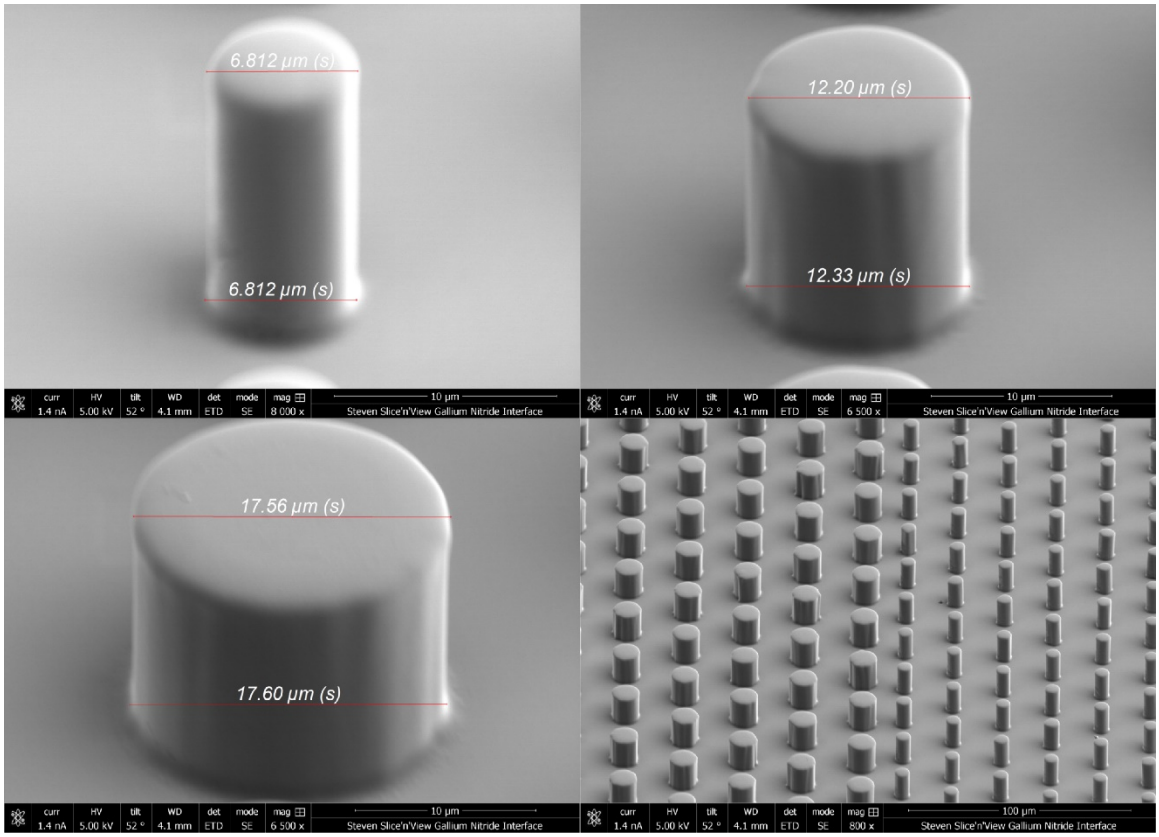

Figure 3.3: Electron microscope (EM) images of typical SU-8 polymeric pillars within our microfluidic devices. Pillar radii were measured using EM images for subsequent experiments (chapters 4-5).

After the SU-8 was exposed, it was heated at 95°C for four minutes to complete polymerization of the exposed photoresist. Samples were then placed in SU-8 developer and mildly agitated (stirred) for three minutes, dissolving the unexposed (non-polymerized) SU-8 photoresist, and thus leaving only the exposed structures. The sample then underwent a 'hard bake' at 200°C for 10 minutes to increase structural stability.

3.4 Novel Fabrication Method: PDMS Gasket and Sealing

Next, the cover piece, which sealed the patterned device, was made using a thin layer of PDMS bonded to a glass slide. The glass slide first had inlet and outlet ports (~1.5 mm) drilled through it using a diamond drill bit submerged in water (to eliminate airborne powdered glass). The drilled slide was then thoroughly cleaned by sonication in acetone for 10 minutes, then rinsed with isopropyl alcohol (IPA), dried using nitrogen gas, and finally baked in a UV ozone oven for one hour at 150°C to remove remaining microscopic organic matter. Liquid PDMS was deposited on the surface and then sandwiched between the drilled slide and another, treated glass slide. Thin spacers (~100 um) were placed at the corners of the treated class slide ($1cm$ x $1cm$ squares of packing tape at each corner). To ensure that the PDMS bonded only to the drilled slide, the spacer slide was treated with trichlorosilane, which, as described earlier, reduces adhesion to PDMS. Treated slides were placed in a closed petri dish with a 1 μL drop of trichlorosilane on a separate glass slide and left in a chemical hood (trichlorosilane must be handled with care as it is both volatile and toxic). Overnight, vapors deposit trichlorosilane onto the glass. The PDMS was then prepared (mixed and degassed) and poured onto the spacer slide. The drilled slide was then compressed onto the spacer/PDMS slide, and the 'sandwiched' three-layer structure was cured in an oven at 100°C for ~1 hour. The drilled slide with bonded PDMS was then removed from the spacer slide using a razor blade inserted at the corners with extreme care, as drilling the inlet/outlet holes reduces the structural integrity of the glass slide. Excess PDMS was then removed from the inlet-outlets with a 1 mm biopsy punch (VWR) and these holes are covered using press-fit tubing connectors (Grace Bio-Labs).

When preparing the device for use, the inlet and outlet ports of the patterned surface were aligned with the drilled holes and compressed by hand with moderate finger pressure. This created a relatively weak but sufficient seal that was long-term stable when negative pressure was applied across the two ports. Flow through the device was achieved by inserting 1.59 mm OD / 0.305 mm ID PTFE fluidics tubing (Grace Bio-Labs) directly into the press fit connectors, with the inlet line connected to the cell suspension and the outlet line connected to a sterile syringe. For crude control, the syringe was pulled manually, or for precise constant flow rates, the syringe was placed in a syringe pump. Once the microfluidic device was loaded with cell suspension, we halted any global flow within the device by disconnecting the lines and sealing the ports with lab tape. Devices made on a silicon wafer substrate could only be imaged using fluorescence microscopy as the wafer substrate is optically opaque and the bright-field source is superior to the device.

After use, silicon devices were easily cleaned for reuse. The devices were pulled apart and each half was rinsed with bleach to remove cells, rinsed with DI water, sprayed with acetone, then IPA, and finally blow dried room-temperature with filtered air. Frequently, features patterned onto a glass substrate do not adhere strongly enough and are destroyed when the device is taken apart, and thus are not suitable for reuse.

3.5 Mask Fabrication

Photomasks are generally either patterned chromium on a quartz or soda-lime-glass substrate, or a thin plastic sheet on which the pattern is printed in black ink. Film masks are significantly cheaper and can be ordered quickly but offer a minimum resolution of 10-30 μm features. Chromium masks offer significantly higher resolution but ordering these

is expensive and can take several days to be manufactured. Chromium masks on a quartz substrate allow for single-micron resolution and high broadband transmittance of light. Fortunately, we were able to fabricate our own masks in the University of Oregon's shared equipment facility CAMCOR. In a relatively simple process we were able to fabricate new device-design prototypes in a single day. A blank quartz mask consists of the quartz substrate and a thin chromium layer covered with AZ photoresist (Merck KGaA); a positive photoresist commonly used for thin ($< 1\ \mu m$) photolithography. The AZ photoresist was exposed at 140 mJ/cm^2 with a 420 nm laser using a SUSS MicroTec LI6 Laser Imager, which yields single-micron feature resolution. The exposed photoresist was then lifted off with AZ 7226 MIF developer, leaving exposed chromium in the intended areas. The exposed chromium was then wet etched, a process to which AZ is highly resistance. After leaving exposed quartz and developed AZ photoresist with chromium underneath. Finally, the remaining AZ was rinsed off with acetone, leaving a negative chromium image of the original exposure on quartz; that is the final photomask.

3.6 Conclusion

This novel technique for microfluidic device creation by no means replaces soft lithography, as, for instance, it eliminates the possibility of multilayer microfluidic devices required by many complex designs. However, it does enable the creation of devices that are valuable in certain experimental contexts. The increased stiffness of the device allows for millimeter (and possibly larger) gaps between features without device collapse. Structures fabricated directly with photoresist enable fabrication of tall ($h > 10\ \mu m$), small ($R < 5\ \mu m$) features, with which bacteria can interact. Development and iterative design of

these new devices was a lengthy process that ultimately led to the high-throughput and high-precision experiments presented in the following chapter.

CHAPTER IV

BACTERIA SCATTER OFF SMALL HIGH CURVATURE SURFACES VIA NON-HYDRODYNAMIC STERIC INTERACTIONS

This chapter contains co-authored material; it has been adapted from K. Hoeger, T. Ursell, "Scattering of Rod-like Swimmers in Low Reynolds Number Environments" currently in submission at Nature Physics. In this work, I contributed to designing the research, performing the research, analyzing the data, and writing the paper.

4.1 Introduction

Microbes inhabit chemically complex and physically anisotropic environments – like wet soils or a mammalian gut – often using self-propulsion to find resources and expand into new territory. In these low Reynolds number settings drag quickly dissipates kinetic energy into heat, such that microbes must continually propel themselves to maintain persistent forward movement, and thus their kinematics conserve neither momentum nor energy. Across multiple length scales, swimming microbes interact with their physical environment in ways that alter their trajectories [14], [15], [30], [34], [50], [91]–[93]. For instance, hydrodynamic forces near surfaces potentiate relevant biological phenomena including cell adhesion [94], biofilm formation [95], [96], or colonization of medical devices like catheters [11], [12]. These physical interactions also present opportunities for influencing the motion of micro-swimmers using micro-fabricated environments [75], [97]–[99], for instance to deflect cells from surfaces [100], to passively concentrate them

in certain regions [17], or to enhance their motility via flow [101]. *Sipos et al.* [30] used micro-fabricated pillars to show that when swimming near convex surfaces with sufficiently small curvatures, hydrodynamic forces 'trap' cells in ~2D trajectories within ~1 cell diameter of the surface. Similarly, bacteria propelled by helical (and hence chiral) flagella have been observed to swim in approximately constant-curvature trajectories staying close to flat surfaces for minutes at a time [102], with the direction of trajectory rotation linked to flagellar helicity [16]. However, above a critical curvature, entrapment decreases, and for pillars of radius less than ~50 μm the fraction of trapped cells rapidly decreases to zero [30]. Further, such surface trapping was reduced by collisions with small colloids (r = 1.5 μm), which increased the rate of forward scattering and hence increased trajectory persistence [34].

Current theory describes swimming cells as force dipoles with a surrounding toroidal 'Stokeslet' flow field [28] extending more than 10 μm from the cell surface, thus trajectory alterations that arise from interactions with steric obstacles are thought to be primarily hydrodynamic [31]. Model predictions vary due to differences in physical and geometrical assumptions, but generally reproduce the attractive trapping exhibited by low-curvature surfaces. However, it is unknown whether such models accurately describe alterations in trajectories upon interaction with small obstacles on the order of 1 to 10 cell lengths. These size scales are relevant, for instance, in (wet) soil types where measured particle-size distributions indicate that the majority of particles (by number) with which a swimming microbe will interact are less than 10 cell lengths [35], [36]. Further, experimental results from [34] suggest that interactions with particles in the 1-10 cell length

range lead to scattering angles that are significantly smaller than those predicted by hydrodynamic models in similar geometries [31], [32].

Thus, while interactions with high curvature surfaces favor forward scattering, the relative roles of hydrodynamics and sterics in the switch between entrapment and forward scattering remain unclear. In this work, we probed high-curvature scattering by imaging hundreds-of-thousands of interactions between flagellar-propelled fluorescent *Escherichia coli* and convex surfaces with positive curvature between 1 and 10 inverse cell lengths. We fabricated microfluidic devices in which bacteria swam among arrays of vertical pillars ranging in size from R = 3.4 μm to 31 μm. We computationally analyzed images to identify trajectories of individual bacteria and characterized scattering events by their impact parameter with respect to a pillar's center. With that data, we calculated the probability distribution of scattering angles for the range of impact parameters $-R \leq b \leq R$. We did not observe hydrodynamic trapping in this range of convex curvatures, but we did observe forward scattering across all measured impact parameters and radii. Across the range of pillar sizes tested, we found that the measured mean scattering angle, exit angle, and interaction time was in quantitative agreement with a relatively simple, fit-free sterics-only model. Our data support a hybrid sterics-hydrodynamics framework for understanding – and potentially controlling – swimmer-surface interactions. Together with previous work, our results underscore that in real-world environments – like ocean particulates [13], soils [35], [36], or a mammalian gut [26], [103] – micron-scale objects influence microbial motion, with potential effects on navigation and subsequent resource acquisition. Further, a physical understanding of how steric objects alter microbial trajectories presents

opportunities to design environments that control and/or affect their movements and resulting population dynamics.

4.2 Characteristics of cell scattering from high curvature pillars

As cells navigate through real-world environments, like wet sediments or a mammalian gut, they encounter solid, steric objects that alter their trajectory due to both hydrodynamic and steric forces. We wanted to understand the relative role that steric forces play in altering bacterial trajectories at scales about the length of a cell (3.75 μm) to about 10 cell lengths. We built microfluidic devices that present swimming cells with an array of micro-fabricated steric pillars with sizes ranging from R = 3.4 to 31 μm. Cells were cytoplasmically labeled with GFP and their motion was imaged using a fluorescence microscope (see 4.X Methods). We imaged hundreds-of-thousands of interactions between swimming bacteria and these steric pillars. To each trajectory we applied custom object tracking algorithms to measure the impact parameter, $\boldsymbol{b}$. We then calculated the outgoing trajectory vector and compared the angle between incoming and outgoing vectors to calculate the scattering angle θ (Fig. 4.1A/B). In Figs. 4.1, 4.3, and 4.8 C-E we show data for $\boldsymbol{R}$ = 8.3 μm; data for other pillar radii are shown in figure 4.2, 4.9, and 4.10.

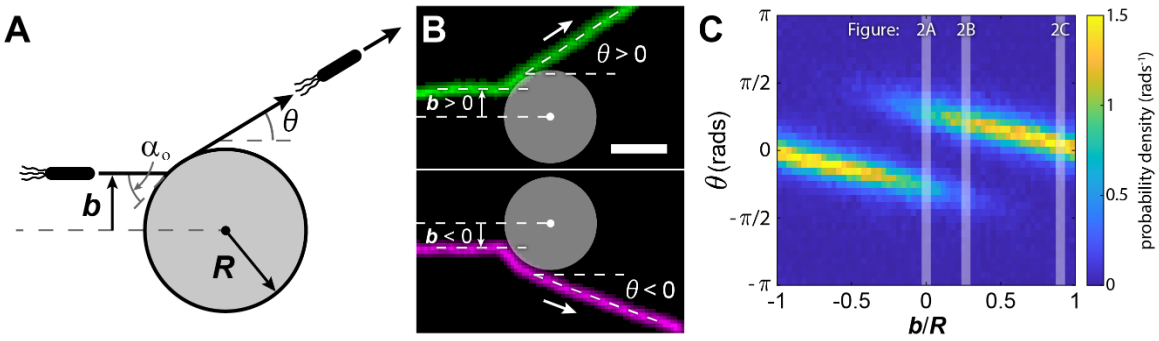

Figure 4.1: (A) Schematic showing the impact parameter b for a cell impacting a pillar of radius R at an angle α_o and then scattering from the pillar with an outgoing angle θ. As it slides along the pillar surface, the cell rotates and leaves contact with the pillar when its direction of motion, characterized by α, is tangent with the pillar surface, leading to a scattering angle θ. (B) Examples of maximum intensity projections of bacterial trajectories interacting with a pillar (drawn in grey) for clockwise (green) and counter-clockwise (magenta) paths. The arrows indicate the direction of movement and the scale bar is 10μm. (C) Heat map showing probability density per radian of an interaction yielding a scattering angle θ for a given dimensionless impact parameter (b/R), here R = 8.3 μm. Each column is a normalized distribution. Cells with positive impact parameter tend to slide around the pillar in the CW direction leading to a positive scattering angle (right lobe), while cells with negative impact parameter tend to slide CCW leading to a negative scattering angle (left lobe). A small fraction of trajectories for each lobe traverse the pillar with the 'opposite' handedness (e.g. right lobe for b/R < 0). Fig. 2 examines the scattering distributions for the indicated values of b/R (light vertical bars).

For each range of the impact parameter we classified trajectories as either going clockwise (CW) or counter-clockwise (CCW) around the steric pillar, producing normalized probability distributions for scattering angle. The sum of the CW and CCW scattering angle distributions for $\boldsymbol{R}$ = 8.3 μm is shown in Fig. 1C. These distributions exhibited common characteristics across all measured pillar radii. The two 'lobes' of the probability map are produced by the two chiral directions of motion, with the majority of CW paths corresponding to positive impact parameter and the majority of CCW paths corresponding to negative impact parameter (Fig. 4.1B/C). Each lobe has a negative slope,

where increasing the magnitude of $\boldsymbol{b}$ monotonically decreases the mean scattering angle, which is almost always acute. As the impact parameter approaches the object size ($|b| \rightarrow R$) the mean scattering angle approaches, but does not cross, zero, consistent with a lack of hydrodynamic trapping. We are not aware of previous hydrodynamic models that examine our exact scattering geometry (i.e. an upright cylinder between two large, flat surfaces), however, hydrodynamic models of force-dipole swimmers interacting with spherical obstacles (i.e. a similar geometry and similar length scale) [31] predict a wider range of angular deflections that cross $\theta = 0$. Further, we observed that the maximum mean scattering angle increased with pillar radius (SI Fig. 5), which is in contrast to hydrodynamic models that predict longer interaction times, and hence smaller scattering angles for increasing radius of curvature [31]. Likewise, the observed behavior differs from the longer interaction times during surface trapping around flat or low curvature objects [30].

Consistent with previous measurements [34], the vast majority of steric interactions led to forward scattering ($-\pi/4 < \theta < \pi/4$). However, when $\boldsymbol{b}/\boldsymbol{R}$ was positive we measured a significant (minority) fraction of swimmers that rotate CCW, extending the CCW-rotator distribution beyond the $\boldsymbol{b}$ = 0 centerline, with that fraction decaying to 0 as $b/R \rightarrow 1$ (Figs. 4.1C and 4.3).

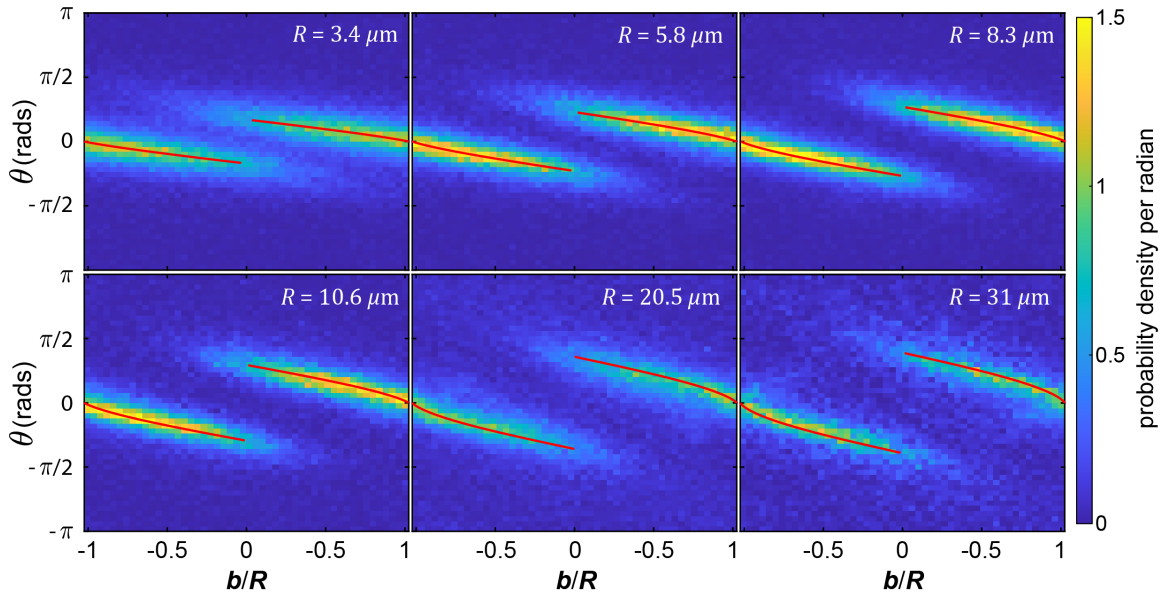

Figure 4.2 Column normalized scattering angle distributions as a function of dimensionless impact parameter ***b/R***, for all pillar radii measured. We see the characteristic double lobe corresponding to CW and CCW motion around the pillar. The separation between lobes increases with pillar radius. For the two largest pillars, noise begins to dominate as we have significantly few interactions captured. The red lines show the predictions from our sterics-only model.

Similarly, when $\boldsymbol{b}/\boldsymbol{R}$ was negative we measured the same effect mirrored across the $\boldsymbol{b} = 0$ and $\theta = 0$ lines. In either case, we refer to these as 'counter-rotator' trajectories – these forward scattering events correspond to trajectories that traverse the pillar the 'long way' around. We discuss a potential mechanism underlying this effect in the modeling section below.

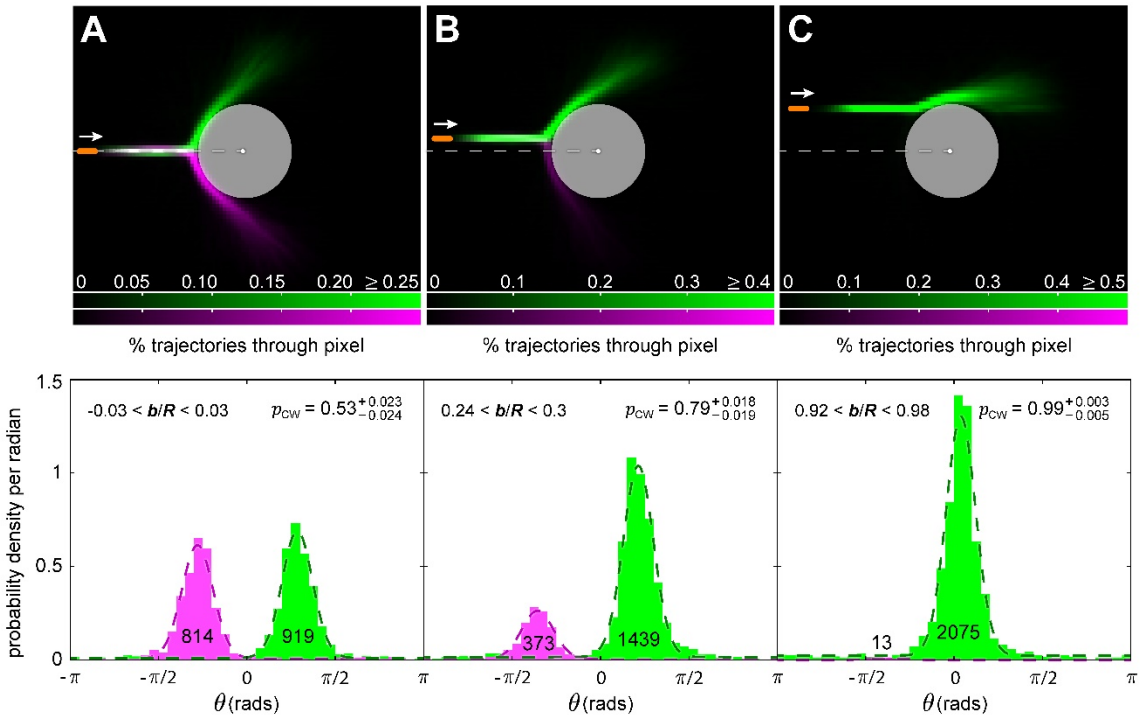

Figure 4.3: Each column (A, B, C) shows the aggregated scattering data for ~2000 interactions for different values of $\boldsymbol{b}/\boldsymbol{R}$, as indicated on the plots on the bottom row. (top row) Aligned interaction trajectories for a bacterium (shown approximately to-scale in orange) scattering from a pillar with $\boldsymbol{R} = 8.3\ \mu m$. Green trajectories / histograms correspond to CW paths and magenta trajectories / histograms correspond to CCW paths. In the top row, the color intensity reports on the fraction of trajectories that passed through a given pixel; color saturation was chosen to show a maximum fraction of all trajectories. (bottom row) Each plot shows the normalized distribution for CW (green) and CCW (magenta) scattering angles, with the number of trajectories written on each distribution. The MLE fits to a modified von Mises distribution are shown as the dashed lines, with corresponding CW probabilities and 95% confidence intervals shown CW in each plot. In general, as $\boldsymbol{b}/\boldsymbol{R} \to 1$, $p_{CW} \to 1$ and $\langle\theta\rangle \to 0$.

In Figure 4.3, we examine the trajectories and chiral angle distributions for three distinct ranges of the impact parameter, again for $\boldsymbol{R}$ = 8.3 μm. The top row of Fig. 4.3 shows the probability that a trajectory passed through a given *XY* position (pixel) – in any *Z*-plane – during a scattering interaction, with CW trajectories shown in green and CCW

trajectories shown in magenta. These scattering maps are formed by setting a pixel to one if a trajectory passes through it (zero otherwise) and then averaging over all such binary images for the given range of $\boldsymbol{b}$. This visualizes the general trend between b/R and θ, the statistical nature of these scattering events (i.e. the 'spray' of trajectories that result from distinct ranges of b/R), and the spatial distribution of counter-rotator trajectories.

For each chiral direction within a narrow bin of b/R the observed scattering angles were well described by a von Mises distribution with a constant offset

$$\rho(\theta; \langle\theta\rangle, \sigma, c) = \frac{c}{1 + 2\pi c}\left(1 + \frac{e^{\frac{\cos(\theta - \langle\theta\rangle)}{\sigma^2}}}{2\pi c I_0(\sigma^{-2})}\right) \quad (1)$$

where θ is the measured scattering angle, σ the width of the distribution in radians (analogous to the standard deviation of a gaussian), $\langle\theta\rangle$ is the mean scattering angle, c is the offset parameter, and I_o is the modified Bessel function of the first kind (Fig. 4.3 bottom row). The offset accounts for the small fraction of cells whose interactions with a pillar lead to a uniform, random scattering angle about the unit circle, referred to in [34] as 'tumble-collisions' (see Fig. 4.4). We used maximum-likelihood estimation to fit the mean, width, and offset parameters for these scattering angle distributions as a function of b/R, and to determine confidence bounds for those parameters (e.g. see Fig. 4.5). Those fits are shown as dashed lines in Fig. 4.3 bottom row. We calculated the fraction of trajectories that scattered CW (p_{CW}) as a function of impact parameter, and found a smooth and chirally symmetric transition from majority CCW to majority CW as b/R increased from -1 to +1, with larger radii producing a steeper transition (see Fig. 4.6). In the bottom row of Fig. 4.3 we show the corresponding values of p_{CW} with 95% confidence bounds. For each binned

range of *b/R*, the width of the scattering distribution was approximately constant (~0.3 radians across all data) and chirally symmetric (see Fig. 4.7). There are likely multiple factors that contribute to this spread in scattering angle, including: rotational and translational diffusion of the cell as it swims; variations in cell length, shape, and axis-of-propulsion; micro-scale surface roughness; and imaging imprecision. Distinct from those sources, the model described below offers a quantitatively consistent mechanism for the observed spread in scattering angle across $\boldsymbol{b}/\boldsymbol{R}$, that relates to the existence of the counter-rotator trajectories.

4.3 Modeling Cell Scattering

Hydrodynamic forces are known to significantly alter bacterial trajectories near flat and low-curvature surfaces [16], [30]. We wanted to know if steric forces alone could account for the observed interactions between swimming cells and steric pillars. We developed a model that adheres to the following assumptions: (i) hydrodynamic forces and torques between swimmer and pillar surfaces are negligible, (ii) friction between cell and pillar surfaces is negligible (see SI), (iii) the cell is propelled from the rear by a fixed propulsion force $\boldsymbol{F}$, in-line with its long-axis, (iv) the cell is a thin ($R_{\mathrm{cell}}/L \ll 1$) stiff rod of length $\boldsymbol{L}$, measured from the center of its flagellar bundle to the cell tip [30], (v) free-swimming motion has a persistence length much larger than the interaction zone, and (vi) that forces that generate rotation of the cell in the plane of the microfluidic device ($\boldsymbol{F_R}$) are due to contact between that cell and the solid pillar.

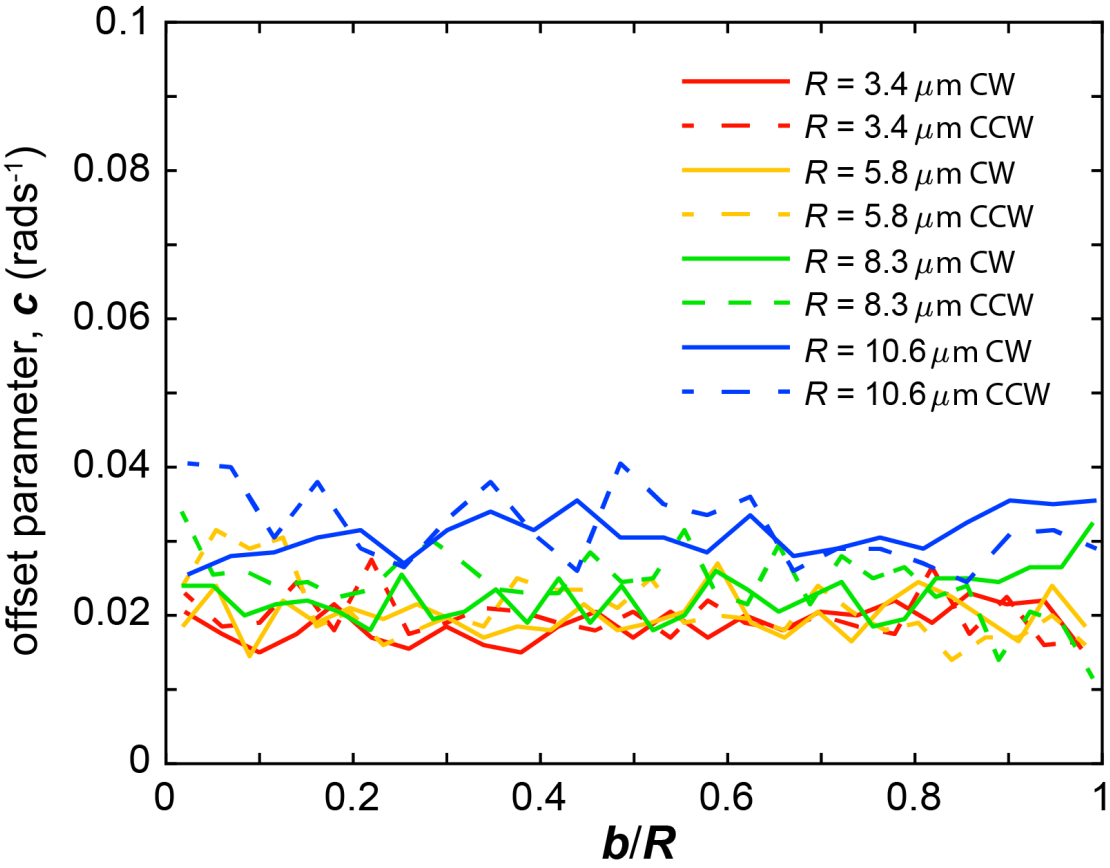

Figure 4.4: Plot of the von Mises offset parameter (called c above) as a function of b/R across the four smallest radii. The data are the modes from the MLE fits for the parameter estimation. The offsets are roughly constant across |b/R| and approximately chirally symmetric, indicating that the frequency of random scattering events is independent of |b/R| and not related to direction. There is also a rough upward trend in the offset with increasing pillar radius, indicating that random scattering is more common around larger pillars. This may be related to the fact that larger pillars correspond to longer interaction times, and hence a higher probability of a random event (e.g. chemotactic tumble) during the interaction. It may also result from increased hydrodynamic trapping at larger radii, which causes cells to follow trajectories around the pillar for much longer times than steric scattering, but with a random detachment time, and hence random angle.

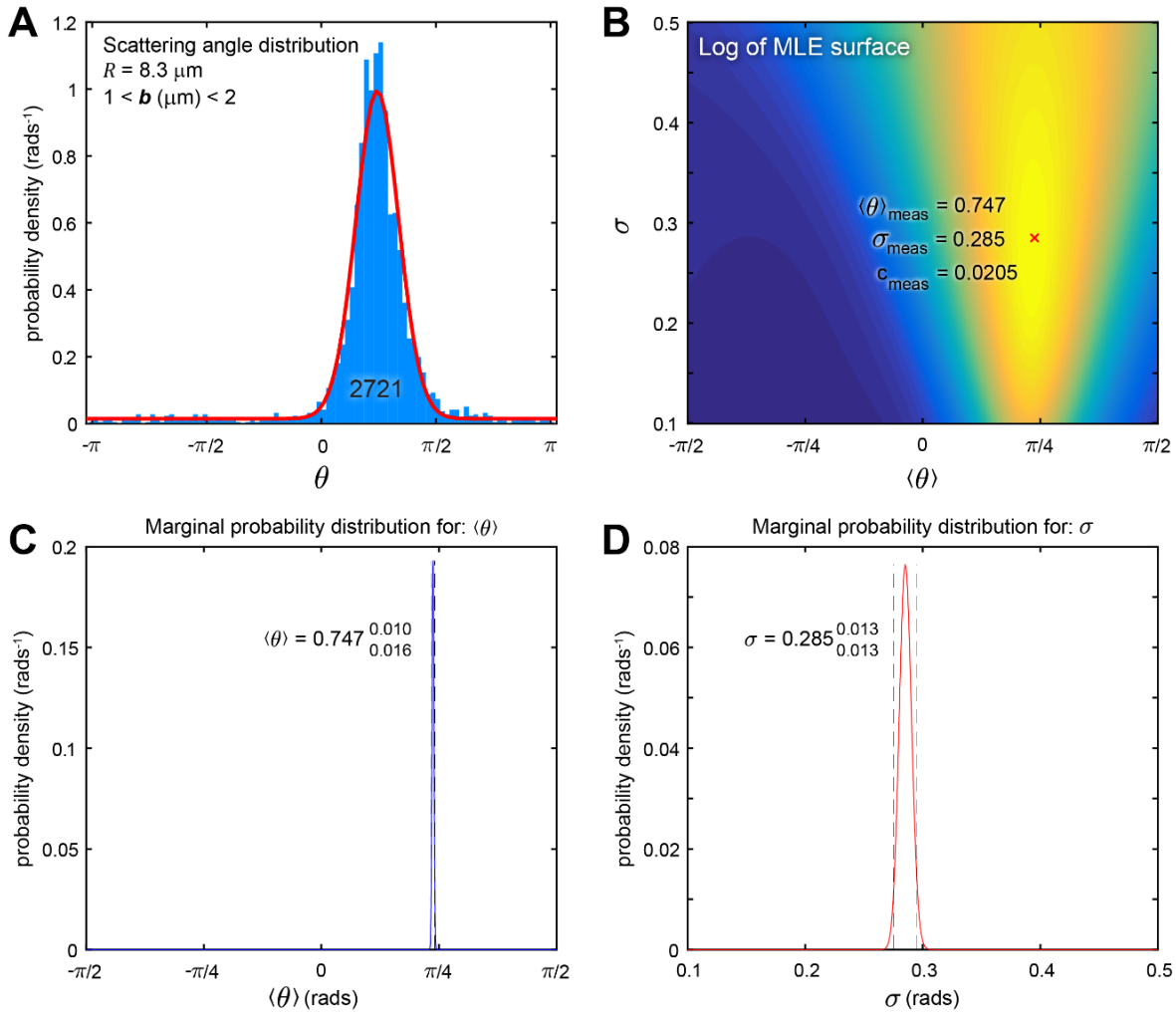

Figure 4.5: Example output of the MLE fitting. (A) A CW chiral scattering distribution with the MLE fit in red. (B) The natural log of the MLE fit surface for all data in the histogram, showing the mode values for all fit parameters. (C) The probability distribution for the measured value of hθi showing the mode and 95% confidence interval. (D) The probability distribution for the measured value of σ – the width of the scattering distribution – showing the mode and 95% confidence interval.

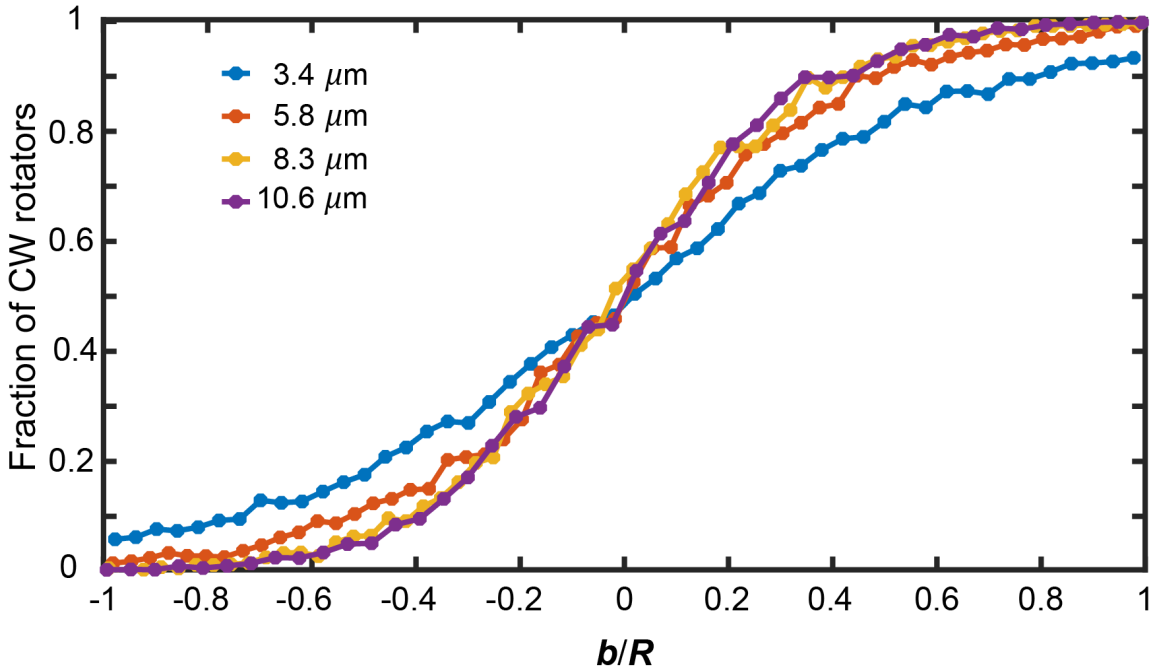

Figure 4.6: Fraction of cells that rotate clockwise around a pillar as a function of dimensionless impact parameter. Assuming the pillar is centered on a local Cartesian coordinate system, clockwise rotation was defined by cell trajectories that crossed the center-line (x = 0) with y > 0 in the rotated frame. The I expectation from the steric model is that this would be an increasing step-function at ***b/R*** = 0. Based on visual inspection of imaging data, as well as quantitative analysis of breaking the model assumption that the initial contact angle (α_o) is set purely by ***b***, ***R***, and δ, we hypothesize that fluctuations in cell orientation upon impact are what produce trajectories that traverse the pillar the 'long way' around (i.e. opposite to the chirality predicted by the steric model). Such fluctuations are caused by translational and rotational diffusion of the cell body, as well as variations in cell morphology that affect initial contact angle. If those fluctuations in orientation due to diffusion and morphology are rotationally isotropic, then we expect (and observe) that these curves are symmetric upon flipping about ***b/R*** = 0 and p_{cw}= ½, regardless of radius.

Typical Reynolds numbers for swimming bacteria are $10^{-4} - 10^{-3}$, indicating that a constant propulsion force results in a constant cellular velocity (here measured to be ~23 μm/s from the mean free-swimming speed).

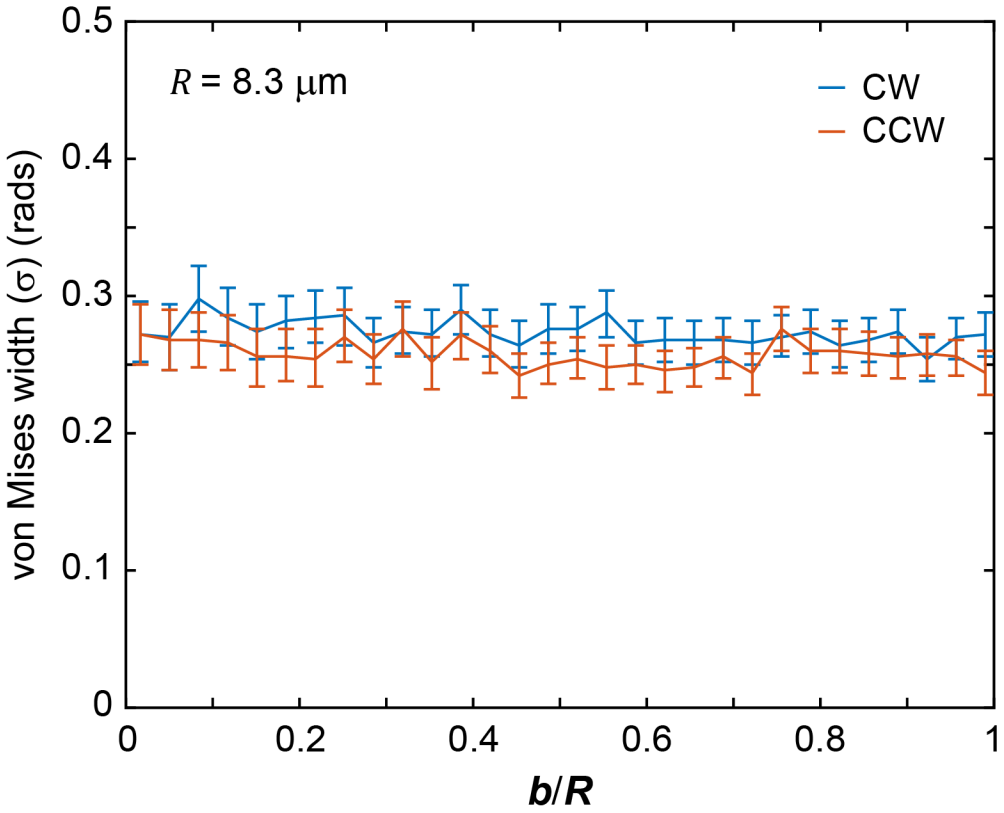

Figure 4.7: Plot of the von Mises width parameter (called σ above) as a function of b/R for R = 8.3 μm. The data are the modes from the MLE fits and the bounds are 95% confidence intervals on the parameter estimation. The width parameter is approximately constant across all values of b/R and is approximately chirally symmetric.

We model the drag force on each end of the cell by a spherical Stokes drag with particle radius equal to cell radius (0.5 μm) and fluid viscosity equal to that of water. The length of the cell $\boldsymbol{L}$ does not change and so its motion is completely described by the motion of each end point $\boldsymbol{P_1}$ and $\boldsymbol{P_2}$ which are parametrically described by ($x_1(t)$, $y_1(t)$) and ($x_2(t)$, $y_2(t)$). Assuming that viscous drag is the primary constraint on motion, we assume that all velocities are proportional to net force with a fixed mobility $\boldsymbol{\sigma}$.

$$v = F\sigma \tag{2}$$

The propulsion force F, independent of any state of motion can be decomposed into a component that is parallel to the scattering surface $\boldsymbol{F}_{||}$ and a component normal to the surface $\boldsymbol{F}_{\perp}$, such that given the angle between the cell orientation and tangent surface $\boldsymbol{\alpha}$:

$$\mathrm{F}_{\perp} = \mathrm{F}\sin(\alpha) \tag{3}$$

$$\mathrm{F}_{||} = \mathrm{F}\cos(\alpha) \tag{4}$$

We set the coordinate origin to the circle's center and hence

$$\mathrm{x}_2 = -\mathrm{R}\cos(\phi) \tag{5}$$

$$\mathrm{y}_2 = \mathrm{R}\sin(\phi) \tag{6}$$

and thus

$$\dot{\mathrm{x}_2} = \dot{\phi}\mathrm{R}\sin(\phi) \tag{7}$$

$$\dot{\mathrm{y}_2} = \dot{\phi}\mathrm{R}\cos(\phi) \tag{8}$$

Using the parallel force we can also write:

$$\dot{\mathrm{y}_2} = \mathrm{F}_{|}\sigma\cos(\phi) = \mathrm{F}\sigma\cos(\alpha)\cos(\phi) \tag{9}$$

$$\dot{\mathrm{x}_2} = \mathrm{F}_{|}\sigma\sin(\phi) = \mathrm{F}\sigma\cos(\alpha)\sin(\phi) \tag{10}$$

These equations both dictate that

$$\dot{\phi} = \frac{\mathrm{F}\sigma}{\mathrm{R}}\cos(\alpha) \tag{11}$$

with the initial condition related to the impact parameter by

$$\phi_{\mathrm{o}} = \sin^{-1}\left(\frac{\mathrm{b}}{\mathrm{R}}\right) \tag{12}$$

and the initial value of α is

$$\alpha_o = \frac{\pi}{2} - \phi_o \tag{13}$$

because we assume the cell impacts in a flat orientation (i.e. $y_1 = y_2$). Then the rate of change of α due to mechanical torque is

$$\dot{\alpha_T} = -\frac{F_R \sigma}{L} \tag{14}$$

where

$$F_R = F_{||} \cos\left(\frac{\pi}{2} - \alpha\right) = F_{||} \sin(\alpha) = F \cos(\alpha) \sin(\alpha) \tag{15}$$

And the rate of change of α due to the *surface curvature* is

$$\dot{\alpha_C} = -\dot{\phi} = -\frac{F\sigma}{R} \cos(\alpha) \tag{16}$$

Therefore,

$$\dot{\alpha} = \dot{\alpha_T} + \dot{\alpha_C} = \frac{F\sigma}{L} \cos(\alpha) \sin(\alpha) - \frac{F\sigma}{R} \cos(\alpha) \tag{17}$$

This model predicts that if the cell is perpendicular to the surface ($\alpha = \pi/2$) then $\dot{\alpha} = 0$ and we assume that at this point the microswimmer leaves the surface. We then numerically solve eqn. 17 for α for the time t_f and angle ϕ_f that occur when the cell leaves the surface. From that, the scattering angle is given by

$$\theta = \frac{\pi}{2} - \phi. \tag{18}$$

This model also predicts that there is a non-zero critical angle

$$\alpha_c = -\sin^{-1}(\rho) \rightarrow \rho < 1 \tag{19}$$

that results in a stable orientation with respect to the surfaces, but the fact that this angle is negative means that this only occurs for cells on the 'inside' (i.e. negative curvature), which may be part of the consistent orientation of motile *Bacillus Subtilis* cells observed on the *inside* curvature of a circle [104].

An interaction with a pillar of radius R was computationally triggered when a bacterium came within $R + \delta$ of the pillar center, where δ is the radial zone around the pillar inside of which we measured interactions, usually 2 – 3 μm from the pillar surface. Thus, for a given value of b, the initial straight line path from entry into the interaction zone until contact with the pillar has a length

$$s_1 = R\left[\sqrt{\left(1+\frac{\delta}{R}\right)^2 - \left(\frac{b}{R}\right)^2} - \sqrt{1-\left(\frac{b}{R}\right)^2}\right] \tag{20}$$

which given our assumption of a constant swim speed v gives us a transit time of

$$t_1 = \frac{s_1}{v} \tag{21}$$

and the distance between the cell losing contact with the pillar and the interaction zone exit point is

$$s_3 = R\sqrt{\left(1+\frac{\delta}{R}\right)^2 - 1} \tag{22}$$

which again gives us a transit time

$$t_3 = \frac{s_3}{v} \tag{23}$$

Given the time spent interacting with the pillar t_2 from our numerical solution to equation 17, the total time spent within the interaction zone is

$$\mathrm{t_{tot}} = t_1 + t_2 + t_3 = t_f - t_o \tag{24}$$

which we compare to our data in figure (b vs time). In our data processing, we subtract a constant length of 1 μm from s_1 to account for the offset between the position of the tip which contacts the pillar and the position of the cell centroid. It is worth noting that the assumptions of this model apply to other rod-like microswimmers propelled on-axis from the rear, including abiotic Janus particles [105]. Likewise, while the differential equation above describes the interactions with a convex surface of constant radius, the component of the rate of change of α with respect to the surface (eqn. 17) can be adapted to other convex surfaces.

This model has no fit parameters as cell length is externally known ($L = 3.75\ \mu m$, which accounts for the propulsion force acting from part-way into a typical flagellar bundle [30]), pillar radius is measured from electron microscopy of our microfluidic devices (see Fig. 3.2), the fluid viscosity is that of water, the initial contact angle is directly related to *b*, and the average swim speed is measured with our image analysis (and hence application of Stokes drag gives the average propulsion force ***F***). We used these known parameters and numerically solved eqn. 17 for the interaction time, exit angle (β), and scattering angle (θ). In figure 4.8B, we compare the model predictions for mean scattering angle to measured data across four different radii. In figure 4.8 C-E we compare the measured distributions for scattering angle, exit angle, and interaction time to the model predictions for $R = 8.3\ \mu m$ with other radii shown in figures 4.2, 4.9, and 4.10.

Overall, we find good quantitative agreement between the sterics-only model and the measured scattering distributions over the range $-R \leq b \leq R$, especially for pillar radii $\lesssim 20$ μm. We note, however, that as the radius of the cell approaches the radius of the pillar (i.e. for $R_{\mathrm{cell}} \sim R$) the model assumption of the cell represented by a *thin* stiff rod breaks down for small impact parameters, leading the model to underestimate the scattering angle for small $\boldsymbol{b}$. Likewise, assuming that a cell impacts the pillar surface with its long axis parallel to the incoming scattering vector (e.g. as drawn in Fig. 1A), the steric model predicts all trajectories with $\boldsymbol{b} > 0$ should go CW, while all trajectories with $\boldsymbol{b} < 0$ should go CCW, or said differently, the fraction of CW trajectories would be an increasing, discontinuous step function at $\boldsymbol{b} = 0$. However, as described earlier the existence of counter-rotator trajectories is in contrast to this prediction. Correspondingly, we did not measure a sharp step-function in the fraction of CW rotators vs. b/R, though across all radii that function was chirally symmetric, montonically increasing with b/R, and crossed $p_{\mathrm{CW}} = 1/2$ at $\boldsymbol{b} = 0$, as expected for any mechanism that obeys the relevant symmetries (see SI Fig. 10).

Our model assumed that initial contact angle (α_o) was strictly determined by b/R (i.e. the cell swims straight after entering the interaction zone). To explain the existence of counter-rotator events, we explored the model's predictions when the initial contact angle was offset by an amount $\Delta\alpha$ (see SI Fig. 13A), corresponding to a non-contact rotation of the cell immediately before impact. This approach was motivated by our imaging data, in which we observed cells whose variations in shape and/or axis-of-propulsion caused precession about the long axis as it swam toward a pillar – this produced an overall persistent path, but a 'wobbling' cell axis.

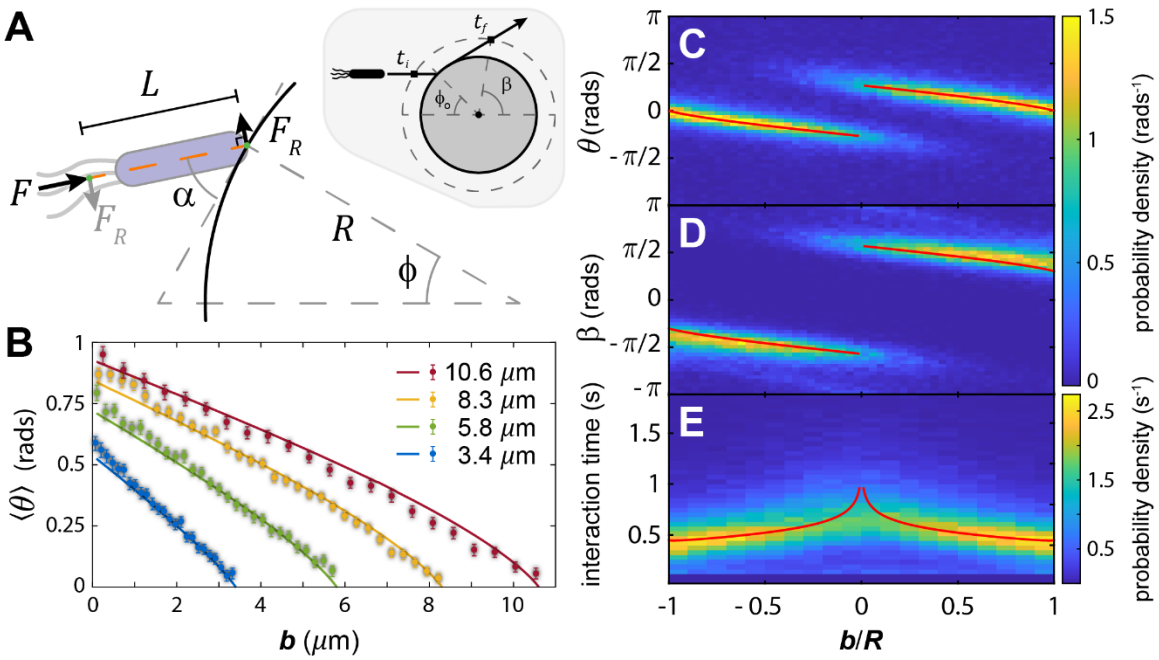

Figure 4.8: Comparing the steric model to experiments. (A) A schematic representation of the forces and geometrical factors described by the sterics-only model. The propulsion force F is generated by the rotation of helical flagella. The length L is the distance – from force-center to cell tip – of the straight, stiff 1D element that F acts on in tangent (orange dashed line). The initial contact angle (αo) is found from the impact parameter b. The model assumes that when the angle $\alpha \rightarrow 0$ the cell ceases to interact with the pillar. The inset schematic shows the relationship between a trajectory and its exit angle β, as well as the interaction time, $t_f - t_i$. (B) ⟨θ⟩ vs. b extracted from MLE fits of the Von Mises distributions with 95% confidence intervals, plotted on top of the sterics-only model predictions with L = 3.75 μm. (C – E) Scattering angle (θ), exit angle (β), and interaction time distributions as a function of dimensionless impact parameter b/R, with R = 8.3 μm. The red lines show the model predictions for the respective measurables.

Likewise, chemotactic tumble events within the interaction zone could also produce such rotations. Lacking specific knowledge about the distribution of $\Delta\alpha$ (our imaging cannot reliably resolve this momentary shift in orientation), we made the simplest assumption – that $\Delta\alpha$ was a flat distribution, symmetric about zero with a single parameter specifying its width.

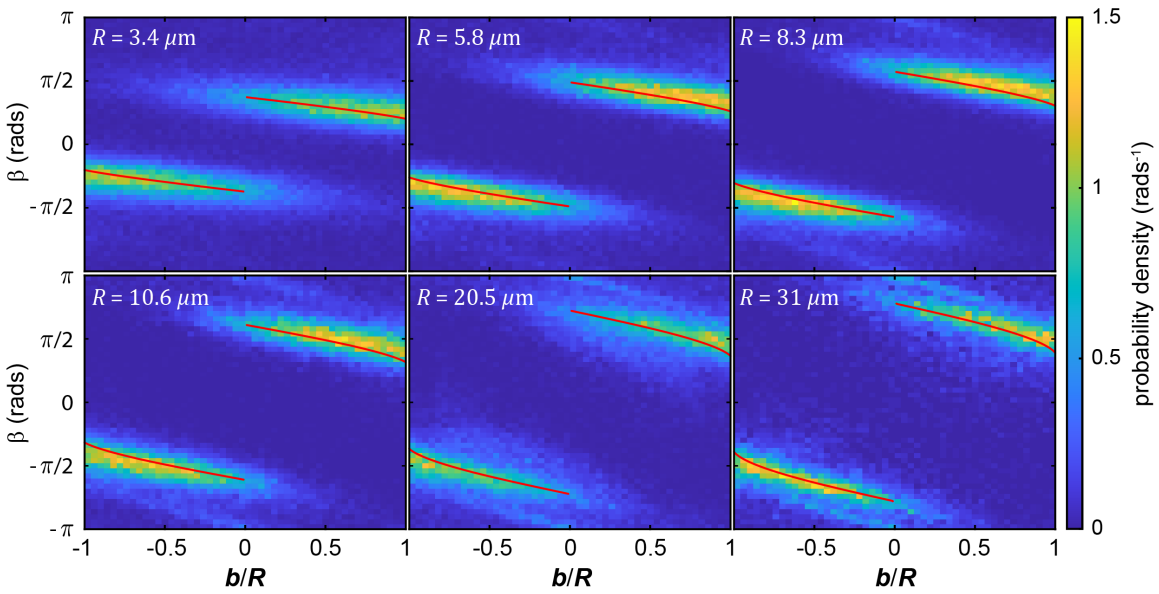

Figure 4.9: Interaction zone exit angle distributions (β) as a function of dimensionless impact parameter b/R, across a range of pillar radii (same type of data as Fig. 3D). The red lines show the model predictions for ⟨β⟩ given the listed radii. Model predictions were calculated by using the first cell trajectory point (in the rotated frame) outside of the interaction radius upon exit. All calculations use the same exogenously specified cell length of L = 3.75 μm. Notably, the 'signal-to-noise' ratio of measured data decreases with increasing pillar radius because the the number of pillars and hence number of interactions we can observe in a single field-of-view decreases faster than R^{-2} .

We chose an angular width of 0.5 radians, or about 1 cell diameter rotating about the cell's center ($L/2$), in either direction. The model predictions for evenly distributed values of $\Delta\alpha$ are shown in SI Fig. 13B for $\boldsymbol{R}$ = 8.3 μm. Laid over the measured data, the model predicts shifts in the chiral discontinuity point in b/R, a distribution of scattering angles that changes with b/R, and concentrations of counter-rotator trajectories that are all consistent with the measured data.

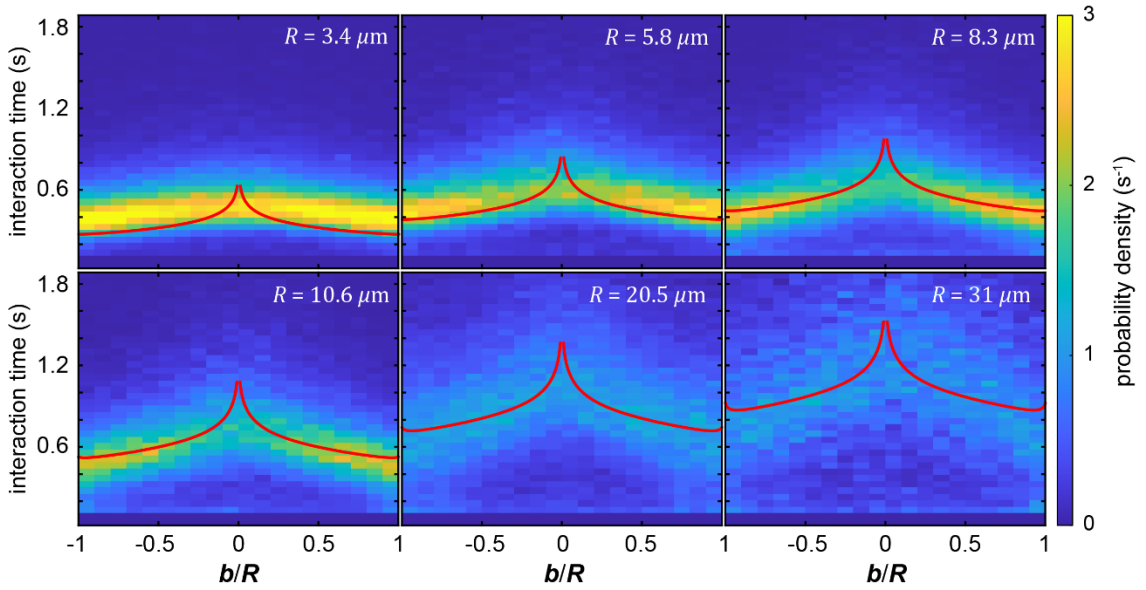

Figure 4.10: Interaction time distributions as a function of dimensionless impact parameter b/R, across a range of pillar radii. The red lines show the model predictions, which were calculated by adding: (i) the transit time from interaction zone entry to pillar contact using the average cell speed, (ii) the time spent in contact with the pillar using integration of the differential equation, and (iii) the transit time from tangency to exiting the interaction zone using the average cell speed. Rotational diffusion shortens the sliding time as trajectories approach b/R → 0, in a way that is not accounted for in the sterics-only model. Notably, the 'signal-to-noise' ratio of measured data decreases with increasing pillar radius because the the number of pillars and hence number of interactions we can observe in a single field-of-view decreases faster than R^{-2} .

For larger pillar sizes ($R \geq 20$ μm), the general trend between impact parameter and scattering angle is well-described by the model, but the model consistently overestimates the mean scattering angle (SI Fig. 14). Our model does not easily account for this effect, but these trends are consistent with scattering interactions from lower curvature surfaces being subject to increased hydrodynamic torque that 'over rotates' the cell during the interaction relative to the steric model.

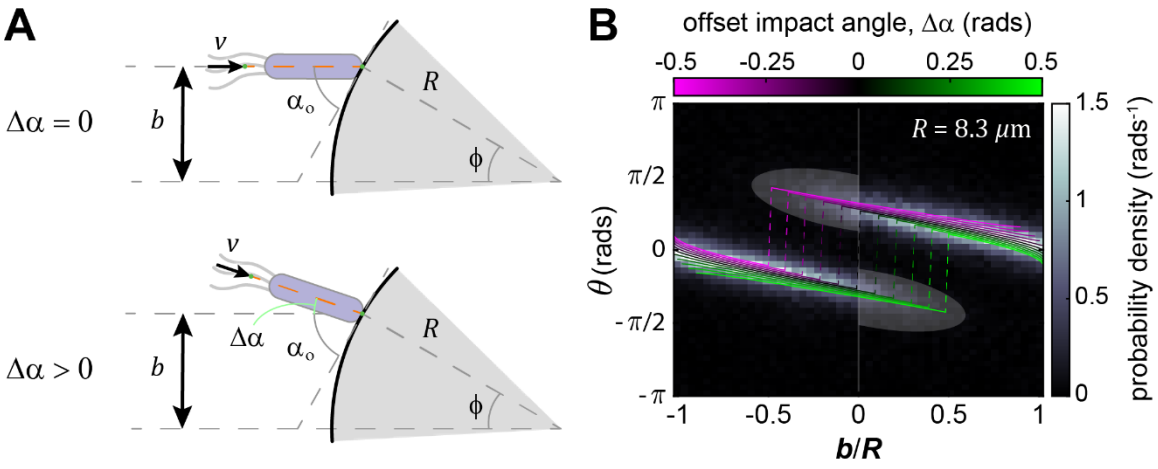

Figure 4.11: Sensitivity of chirality and scattering angle on initial impact angle αo + Δα. (A) Schematic showing the definition of the offset impact angle (Δα). The model fits shown in the main text and preceding figures 4.2, 4.9, and 4.10 assume Δα = 0, in other words that b and R are the only parameters needed to determine α_o. However, all of our scattering data showed trajectories that circumvented the pillar the 'long way' around, that is, with a chirality opposite to what is predicted by the steric model – these are the highlighted lobes in (B). We hypothesized that a combination of rotational diffusion and asymmetries in cellular morphology could lead to significant rotation of the cell body between entry into the interaction zone (which defines b) and contact with the pillar (which defines α_o). We accounted for this possibility in the model by adding a constant offset (Δα) to the initial impact angle (α_o), and then calculated the resulting scattering angle ⟨θ⟩. (B) As an example, we compare these scattering angle functions over a uniform range of offset impact angles (Δα) (see colored lines and legend) to the measured data for R = 8.3 μm. We found that (i) the lobes of measured, atypical chiral probability could be explained by reasonable values of Δα, and (ii) that the observed spread in measured scattering angle for a particular value of b/R could result from the same variations in Δα. Likewise, varying Δα also shifts the discontinuity (dashed vertical lines) along the b/R axis in a way consistent with the observed probability distributions.

For instance, it was shown previously that when cells interact with pillars of radii 20 to 30 μm, hydrodynamic coupling causes a significant fraction of cells (~20%) to be trapped in trajectories that go around the pillar, with interaction times ten-fold longer than our measured interaction times [30]. Thus, our data and model are consistent with the hypothesis that for cells scattering from pillars whose radius of curvature is 1 to 10 cell

lengths and whose cellular geometry meets the thin-rod condition, the forces and torques that govern scattering are primarily steric in origin.

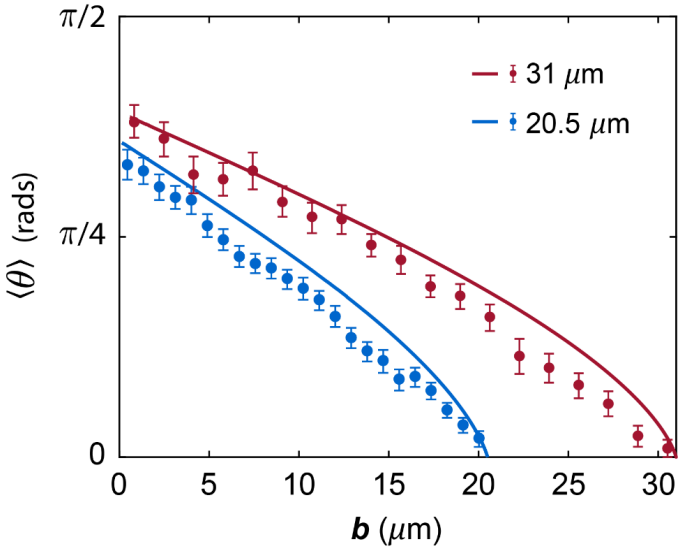

Figure 4.12: Comparison of the model predictions (solid lines) to the measured data for mean scattering angle with 95% confidence intervals around the mean, for the two largest pillars measured. The model overestimates the mean scattering angle at these larger radii, consistent with hydrodynamic forces near these low curvature surfaces over-rotating the cell relative to a sterics-only mechanism, and thus causing a smaller scattering angle.

4.4 Discussion

We measured a primarily forward-scattering interaction between swimming *E. coli* and surfaces with radii of curvature comparable to cell length and generally larger than cell radius, to determine the relative importance of sterics at these length scales. Various aspects of the mean behavior deviate significantly from hydrodynamic models of similar situations

[31], [32] but are well described by a steric model that excludes cell-surface hydrodynamic coupling. This provides strong evidence that swimmers interacting with small, high curvature surfaces are primarily subject to steric forces and that hydrodynamics do not play a significant role in these situations. We did see a significant deviation from our steric model as pillar radii increased, which supports previous experimental findings that hydrodynamic forces play a significant role in describing the motion of bacteria near larger convex surfaces. Taken together, these data suggest that the question of whether swimmer-surface interactions are governed primarily by sterics or hydrodynamics, is one of length scales rather than absolutes.

The sterics-only model makes the additional prediction that swimmers interacting with negative curvature surfaces (concave and where $L/R < 1$) have a stable non-zero contact $\alpha_c = -\sin^{-1}(\rho)$. This effect might be relevant in related studies of the motion of another rod-like flagellated bacterium *Bacillus subtilis* [104]. In that work, swimming cells were contained within a circular hole of radius $\boldsymbol{R}$, effectively presenting the negative curvature analog of a pillar. Their motions were shown to exhibit stable angular orientations with respect to the surface of the circular hole, as measured by the same angle α.

We note that our experimental setup has a number of limitations that cannot be circumvented by straightforward engineering. First, the pillar surface is fully characterized by the radius $\boldsymbol{R}$, but it is also a two-dimensional surface described by two principle curvatures, 0 and $1/\boldsymbol{R}$. It may be that surfaces whose principal curvatures and/or Gaussian-curvature vary produce distinct scattering behavior, potentially (though not necessarily) still well-described by sterics at these length scales. Second, our microfluidic devices had

a depth of ~15 μm which has the advantage of permitting full Z imaging. However, it is worth noting that swimmer-surface hydrodynamic effects depend on fluid dimensions, because the Stokeslet that describes the propulsive flow-field of flagellated bacteria [28] extends >10 μm microns from the cell surface. Third, the three-dimensional nature of the device also means that incoming trajectories toward a pillar are not necessarily strictly parallel with the plane of the device. These non-parallel scattering interactions likely contribute to both the width of the scattering distributions and potentially as an additional source of counter-rotators. Finally, swimming bacteria are known to exhibit hydrodynamically coupled, chiral motion on surfaces [16]; a small fraction of trajectories exhibited this surface-coupled behavior but not in sufficient numbers to influence scattering statistics.

Interaction times from the steric model agree better with measurements as $|b/R| \rightarrow 1$; near $\boldsymbol{b} = 0$, however, the initial contact angle approaches $|\pi/2|$ where the model predicts zero net torque on the cell, resulting in very long interaction times. While the data does not show this spike in interaction times about $\boldsymbol{b} = 0$, this is not surprising because both simple rotational diffusion and/or non-zero offset impact angles ($\Delta\alpha$) remove the portion of the contact trajectory that takes the longest, thus the model tends to overestimate the average interaction time near $\boldsymbol{b} = 0$.

Overall the strong, measured correlation between impact parameter and scattering angle suggests that – regardless of the mechanism – the placement of pillars or other steric objects could be used to alter transport properties of cells that are associated with their trajectory [101]; for instance, net directionality, spatial concentration, path persistence length, or mean-squared displacement. Thus, by choosing appropriate values for object size,

shape, and position, cells may exhibit distinct patterns of trajectories through arrays of steric objects, allowing experimentalists to influence biologically important aspects of cell motion through the design of micro-fabricated environments.

4.5 Methods

Experiments used wild-type *Escherichia coli* (HMMG 1655 parent strain) labeled with cytoplasmic monomeric super-folder green fluorescent protein (GFP) under kanamycin selection. Cells were grown from frozen stock in Luria broth with 50 μg/mL kanamycin for 4 hours at 37°C. In order to control chemical inputs to cellular motility and decrease auto-fluorescence of the media, 25 μL of the liquid culture were diluted into 500 μL of a defined minimal media composed of 10 μM thiamine, 100 mM galactose, and 1 mM each of methionine, threonine, and leucine, in a buffer composed of 0.79 mM magnesium chloride, 45 μM Calcium Chloride, 12 μM Ferric Nitrate, 0.34 mM sodium citrate, 7.6 mM Ammonium Sulfate, 27 mM potassium phosphate dibasic, and 12.8 mM potassium phosphate monobasic. We adjusted the dilution, and hence cell density (1 cell / ~1000 μm^2), so that the majority of interactions were between a single pillar and a single cell. These interactions were imaged in atypical microfluidic devices (described in detail in chapter 3) that supported significantly larger device aspect ratios than are possible in typical soft polydimethylsiloxane (PDMS) lithography devices [106]. Pillars with radii between 3.4 and 31 μm were patterned onto flat silicon surfaces using SU-8 photoresist (Kayaku Advanced Materials Inc.) exposed with a Hoya L-37 long-pass filter (see SI for fabrication details). To cover and seal the device, we cast a ~100 μm layer of PDMS adhered onto a glass slide which was then mechanically compressed onto the patterned substrate for the duration of image acquisition. The increased stiffness of thin PDMS on

glass allowed us to create wide, support-free areas in the device while maintaining a thin fluid layer without the risk of device collapse. Devices consisted of a single chamber 8 mm x 6 mm with a depth of ~15 μm. The device surface was divided into six regions, each patterned with a triangular array of pillars of constant radius with R = 3.4, 5.8, 8.3, 10.6, 20.5, and 31 μm (see SI Fig. 12), and an open control region without pillars. Each pillar was spaced at least 10 μm edge-to-edge from neighboring pillars to ensure that each interaction was hydrodynamically independent of nearby pillars. Before loading cells, we loaded the device with minimal media plus 5% (by weight) Bovine Serum Albumin (BSA) and left for five minutes. This coats the device surfaces with BSA which decreases cell-surface adhesion. The devices were loaded by pulling the diluted suspension of GFP-tagged *E. coli* via a single inlet, single outlet device layout, and subsequently sealing those ports to halt global flow. We imaged bacterial motion at 21.5 frames per second, for 5 – 10 minutes at a time, with an automated Nikon Eclipse TI-E fluorescence microscope using a Plan Fluor ELWD 20x Ph1 ADM objective and an Andor iXon EMCCD camera. This ultrasensitive camera allowed us to capture images with sufficient signal-to-noise at low illuminations, thus minimizing phototoxic effects on cell physiology and motion. The depth-of-field of the 20x objective allowed us to image cells across the entire Z-range of the device. The chamber height constrained cells to move primarily in two dimensions, and thus we did not track vertical motion. Cell segmentation and subsequent XY motion tracking were performed by applying a background-subtracted, standard deviation threshold to identify contiguous pixel blocks and their centroids that corresponded to cells. Around each pillar we defined a zone of fixed width (δ = 2.2 μm); entry of a cell centroid into that zone defined the ‘start’ of an interaction and exit from that zone defined the ‘end’

of an interaction. Valid trajectories (those used in the Results) had 10 *XY* positions (10 time points, ~0.5 s) before entering the interaction zone – these points were used to calculate the impact parameter $\boldsymbol{b}$ – and 10 *XY* positions after exiting the interaction used to calculate exit angle β and scattering angle θ (Fig. 1). Trajectories were further filtered to exclude cases where: (i) more than one cell was in the interaction zone during the duration of an interaction, (ii) the interaction duration was greater than a cutoff (indicative of possible surface adhesion or physiological issues), or (iii) the trajectory was highly erratic upon entry or exit – defined by a threshold in the absolute curvature of the path immediately before entry or immediately after exit, respectively. We collected between ~30,000 and 100,000 valid interactions per pillar radius yielding a roughly even distribution of sampled impact parameters across $-R < b < R$. We validated the entire data acquisition and processing pipeline by measuring trajectories of cells in open regions of the microfluidic device devoid of pillars. We defined fictitious pillars (R_{fict}) and interaction zones and applied our image processing to the motion of cells through those regions. Across the range of impact parameters $-R_{\mathrm{fict}} < b < R_{\mathrm{fict}}$ we measured the distributions of scattering angle, exit angle, and interaction duration for bacterial trajectories, subject to the same filtering requirements discussed above. We then compared the means of the scattering angle, exit angle, and interaction duration to a fit-free free-swimming model of dynamics through the fictitious circular interaction zone, with quantitative agreement between the two (Fig. 4.13).

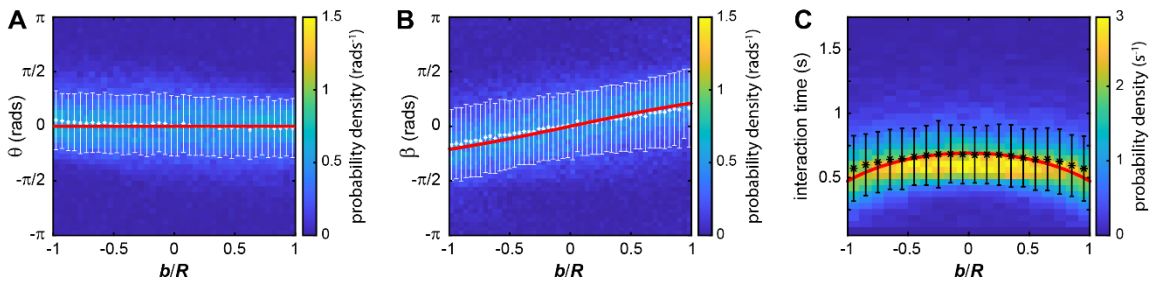

Figure 4.13: Comparison of data and null-model predictions in the case of no steric interaction. We collected imaging data in a featureless area of our microfluidic device and calculated the same relationships for scattering angle (A, θ), exit angle (B, β), and interaction time (C), assuming a nominal fictitious pillar size of R = 5.8 μm with an interaction zone of δ = 2.2 μm. We used the full data collection and analysis pipeline employed with 'real' steric interaction data to this scenario that lacked steric interactions (call this the 'null model'). The null model makes specific, quantitative predictions of the (mean) relationships between dimensionless impact parameter (b/R) and, respectively, scattering angle (θ), exit angle (β), and interaction time. The heat maps are the measured control data, the red lines are the zero-fit predictions of the null model, again assuming the same L = 3.75 μm. The points (white in A and B, black in C) are the means of the measured control data suitable for comparison to the null model. Note that the predictions for ⟨θ⟩ and ⟨β⟩ under the null model are starkly, qualitatively distinct from the predictions of the steric model. These mean values show a mild systematic deviation from the null model as |b/R| → 1 that lies within a standard deviation of the mean of the data (vertical data bars). We speculate that this results from differences in path length and number-density of paths exiting the interaction zone along its circular boundary. Such deviations break the null-model assumption of persistence length λ ≫ (R + δ), producing an asymmetry that progressively grows as |b/R| increases.

4.6 Acknowledgments

We thank Travis Wiles for the gift of the fluorescent *E. coli*, Kara Zappitelli and Kurt Langworthy for guidance on the micro-fabrication, and Benjamín Aleman for sharing equipment. This work was supported by the University of Oregon.

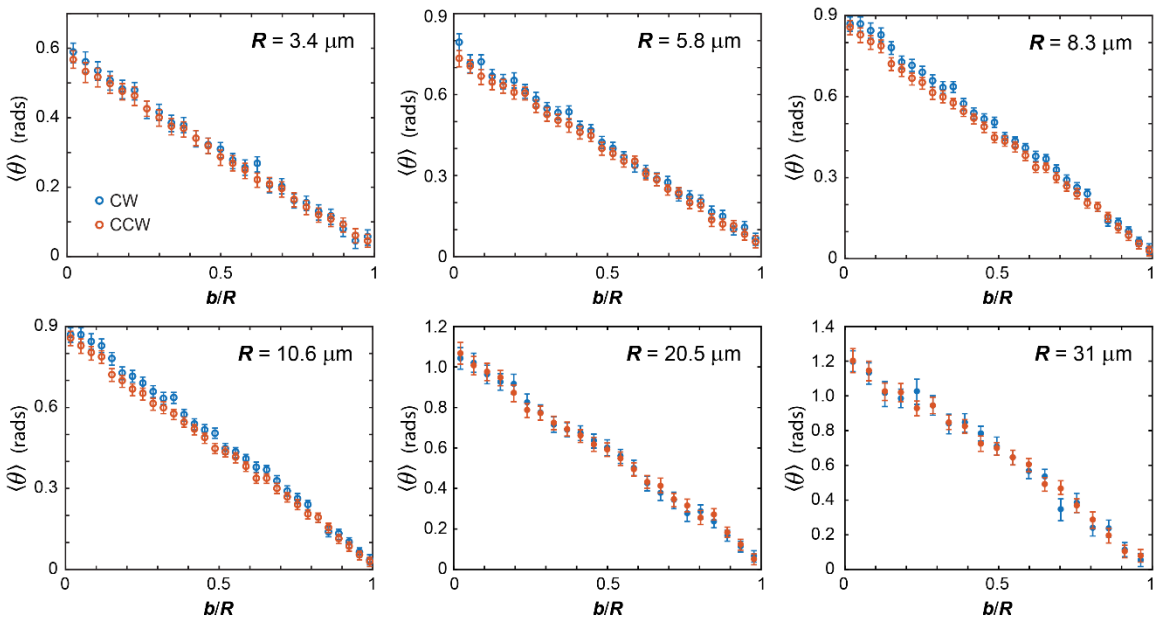

Figure 4.14: Based on the symmetries present in the propulsion of the bacteria and within the microfluidic device, the distribution of scattering angles as a function of dimensionless impact parameter should be – regardless of mechanism – symmetric when mirrored about both the θ = 0 and b/R = 0 axes. Using the MLE fits to a modified von Mises distribution, here we plot ⟨θ⟩ vs. b/R with 95% confidence intervals, with the appropriate mirroring to plot the CW and CCW trajectories overlaid. Across the range of b/R, the data appear approximately symmetric, with mild systematic asymmetry for some radii. These slight chiral asymmetries are likely due to a combination of (observed) systematic asymmetries in the radius of the pillars with height due the fabrication process (see Fabrication Details and electron microscopy images, chapter 3).

CHAPTER V

SCATTERING INTERACTIONS IN OBSTACLE ARRAYS GUIDE BACTERIA

5.1 Introduction: Bacterial Motion in Anisotropic Environments

Bacteria have been found to inhabit a myriad of natural and artificial environments on Earth, from hydrothermal vents in the deep ocean [107], [108], the guts of macro-organisms [7]–[9], and even medical equipment such as catheters [12]. In order to navigate these chemically and physically heterogeneous environments many bacteria rely on self-propulsion to expand their colonies or to traverse up nutrient gradients and down repellent gradients. The physical surfaces these bacteria interact with fundamentally alter the ways in which bacteria move. Pusher-type bacteria that propel themselves by rotating their flagella, hydrodynamically couple to large, flat surfaces causing semi-circular trajectories with radii of curvature typically ~10-20 μm, that persist for tens of seconds to minutes [16], reducing the persistent motion of cells, affecting, for instance, the formation of biofilms on surfaces. On the other hand, patterning a concave boundary on such surfaces reduced cell accumulation on surfaces by more than 50% relative to the flat surfaces [100]. Alternatively, the introduction at low density (2% coverage by area) of small 3 μm diameter spherical obstacles on a flat surface was found to enhance the persistence of surface-bound cells via a forward scattering interaction with the obstacles [34]. It has also been proposed that *E. coli* are able to decrease their tumble rate in environments containing

50 μm square or 50 μm diameter circular pillars in order to maintain their mean rate of motion up an attractant gradient [27].

In our own work (presented in chapter IV) we studied the interaction between swimming *E. coli* and high-curvature convex surfaces and presented evidence and a theoretical model that the underlying physical mechanisms are primarily steric in nature. In that experiment, we observed the effect these interactions had on outgoing cell trajectories as a function of the incoming trajectory. The strong correlation between impact parameter and scattering angle suggests that on lengths much longer than cell or pillar size, the placement of pillars could be used to alter the transport properties of cells associated with their trajectory, specifically their path persistence length and their mean-squared displacement. Thus, by choosing appropriate values for pillar placement and size, cells may exhibit distinct patterns of trajectories through arrays of pillars, allowing experimentalists to shift the balance between ballistic, diffusive, and sub-diffusive motions of swimming cells in different microfabricated environments. To probe the aggregate effects of many such cell-pillar interactions on cell motility, we created devices that contained multiple triangular arrays of pillars across a range of pillar lattice constants and measured cell trajectories within these arrays. We found that the mean squared displacement (MSD) of cell trajectories was largely unaffected by pillars across densities with minor deviations at the highest pillar densities measured. However, we observed that at the highest pillar densities the direction of motion was tightly constrained along particular directions, greatly enhancing the persistence length.

5.2 Methods

To study cell motility in obstacle arrays, we used wild-type *Escherichia coli* (HMMG 1655 parent strain) labeled with cytoplasmic monomeric super-folder green fluorescent protein (GFP) under kanamycin selection. These cells were grown from frozen stock in LB and 50 $\mu g/mL$ kanamycin for 4 hours at 37° C. 10 μL of this culture were then mixed into 500 μL of defined minimal media (described in section 4.5) to control cell density, environmental chemical composition, and to reduce autofluorescence. We used a low cell density ($\sim 10^6\ cells/mL$) in order to minimize cell-cell interactions and thus ensure that measured effects were due to cell interactions with the obstacle arrays. Device surfaces were coated in Bovine Serum Albumin (as described in section 4.5) to decrease cell-surface adhesion. The cellular suspension was loaded into microfluidic devices which were created using the atypical method described in Chapter 3. These devices were approximately $15 \mu m$ deep and were patterned with eight large triangular arrays each spanning a 1mm x 8mm area. All arrays contained pillars with radius $\boldsymbol{R} = 8.3 \mu m$ and each array varied the gap widths (w) between pillar surfaces w = 2, 5, 8, 13, 19, 28, 48, 73μm. These gap widths correspond to pillar densities ρ =0.726, 0.5415, 0.4194, 0.2912, 0.2022, 0.1294, 0.0620, and 0.0324 where ρ is the fraction of area covered by pillars. The device also contained two separate areas each 2mm x 4mm which contained no pillars. We imaged the cells with fluorescence microscopy at ~21.5 frames per second with a Nikon Eclipse TI-E fluorescence microscope using a Plan Fluor ELWD 20x Ph1 ADM objective and an Andor iXon EMCCD camera. Using the 20x objective we were able to image the entire 15µm depth of the device and it gave us a 665 x 665µm viewing frame which allowed us to capture long cell trajectories, with some cells remaining in-frame for hundreds of

seconds. We imaged areas for four minutes at a time with low illumination power to reduce autofluorescence and phototoxic effects on cell motion. We acquired individual cell trajectories using a custom MATLAB data analysis pipeline developed for and outlined in chapter 4.5.

5.3 Bacterial Motility in Arrays

Using the measured cell trajectories, we compared distinct aspects of cellular motility between each array. First, we found that except for at the highest density, the pillar arrays did not have a significant effect on the mean cell speeds when compared to the cells in a no-pillar space (fig. 5.1). For these arrayed areas (and open areas), we found $\langle|v|\rangle \simeq 23\ \mu m/s$,but the cells in the tightest array had $\langle|v|\rangle \simeq 16.5\ \mu m/s$. This drop in velocity is due to frequent interactions with pillars that (as shown in our model in chapter IV) cause a decrease in cell speed during cell-pillar interactions. Similarly, the mean squared displacements (MSD) of cells in the pillar arrays were strikingly similar across gap widths with a small deviation for cells in the 2 μm gap width arrays ($\rho = 0.73$) (Fig. 5.1). We first looked at the scaling of MSD in terms of the power law (t^{α}) at short (t < 1-3s) and long (t > 10s) times. In canonical Brownian motion, at short times, a particle moves ballistically ($\alpha = 2$) on the time scale of the path-persistence length divided by the mean velocity. At long times, the ballistic segments of motion are punctuated by random reorientations that sum to diffusive motion ($\alpha = 1$). As shown in figure 5.1, at small times (t < 3 seconds) we find that the MSD scales ballistically across all but the 2 μm gap arrays including the no pillar control. In the highest density array (2 μm gap), we found that across

these shorter time-scales $\alpha \approx 1.85$, meaning that while the trajectories are super-diffusive at early times, they are sub-ballistic. For all arrays, we found that for moderate times ($6 < t < 20$ seconds) the MSDs were roughly diffusive with $\alpha \approx 1$ (figure 5.1). However, for time scales greater than ~20 seconds, trajectories appeared sub-diffusive with all but the highest density array scaling with $\alpha \approx 0.4$. Cells in the highest density array displayed motion closer to diffusion with $\alpha \approx 0.7$. For the larger gap arrays (and no pillar trajectories), this sub-diffusive behavior is most likely due to the significant fraction of cells which are coupled to one of the two planar surfaces which cause the cells to move in circles. Uncoupled cells, moving in largely straight lines, remain in the viewing frame for 20-50 seconds, thus weighting the long-time population with circular trajectories which appears as sub-diffusive motion in the MSD. It appears that frequent cell-pillar interactions in the highest density arrays ($w = 2 \text{ and } 5\mu m$) suppress the circular motion. As shown in Chapter 4, interactions with small ($R < 20\mu m$) pillars lead to forward scattering (scattering angles $-\pi/4 < \theta < \pi/4$) which is in agreement to the results of a previous study which showed that cells coupled to a planar surface which interact with small spheres overwhelmingly scatter forward [34]. When pillar gap sizes are smaller than the radius of curvature of hydrodynamically induced circular motion, our data suggest that frequent forward scattering events dominate cell trajectories. This is further supported by an analysis of the mean direction of motion displayed by cells within these arrays. Across all MSDs, regardless of pillar density, we see transitions from super-diffusive to diffusive, to sub-diffusive motion which occur at roughly the same times [that didn't make sense as written]. We also saw that apart from the highest density array, all other arrays showed no effect on mean cell speed.

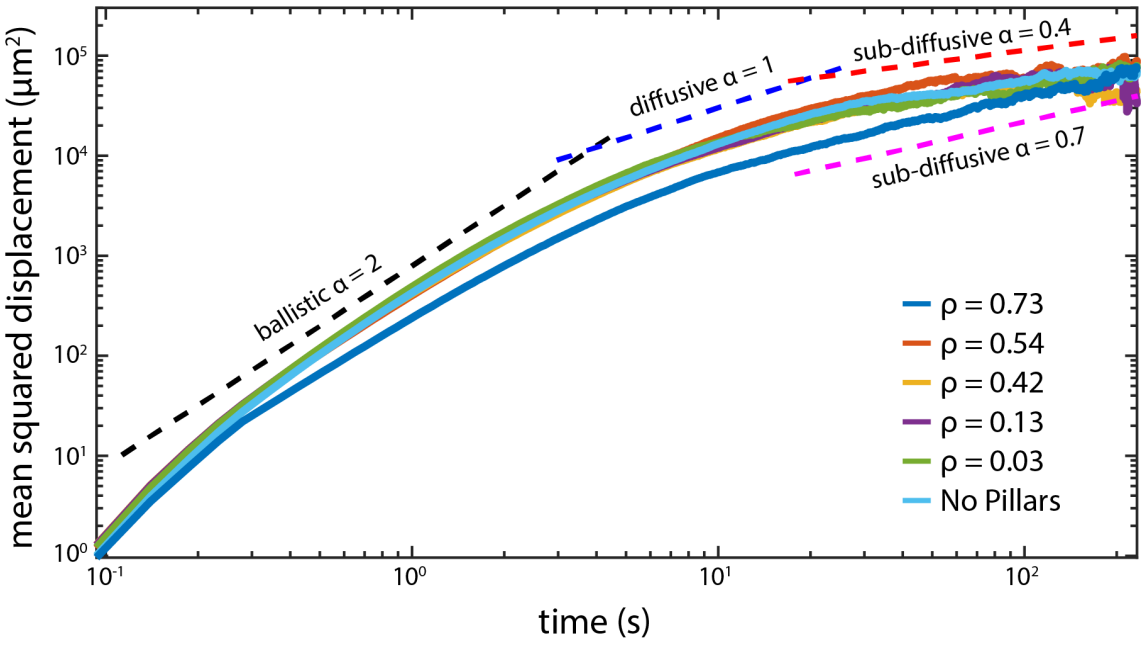

Figure 5.1: Mean-squared displacement as a function of time for cell trajectories in triangular arrays of 8.3μm radius circular pillars with varied pillar densities ρ. We see no major differences in MSD until our maximum density (dark blue line). The difference in mean cell velocity is seen as the gap between the $\rho = 0.73$ array MSD and the rest. MSDs of cells in all spaces are approximately ballistic at small times ($t < 3$s), diffusive at moderate times ($6 < t < 20s$), and sub-diffusive ($\alpha < 1$) at long times ($t > 20s$).

We observed a strong effect on the overall direction of cell movement in high density pillar arrays ($\rho \geq 0.5$). We smoothed cell trajectories with a locally weighted scatterplot smoothing (LOWESS) local regression method using the malowess MATLAB function. From these smoothed trajectories, we looked at the displacement of cell positions that were 20 μm apart in trajectory arclength and found the angle of these displacements in the device reference frame. The probability distribution of the angle of cell displacements shows clear peaks in six directions (fig. 5.2 B) set by our array geometry. We arranged the pillars in a triangular lattice, and thus there are three axes along which cells experience relatively large mean-free paths between collisions, specifically at $\pi/6$,

$\pi/2$, and $5\pi/6$ radians (Fig. 5.2A). At sufficiently high pillar densities, the frequent forward scattering events act to restrict cell motion almost exclusively along these 'crystallographic' directions. In the two highest density arrays, cell movements along these directions ($\pm 5°$) were more than 2.5 times as likely compared to the no-pillar distribution. As pillar density decreases, the scattering interactions decrease in frequency and their directional guiding effects diminish as angular diffusion, run-and-tumble dynamics, and cell-plane hydrodynamic coupling dominate in determining cell trajectories. This is seen in figure 5.2A as the peaks in the movement-angle distribution gradually broaden and decrease in magnitude as pillar density decreases, until the distribution is indistinguishable from the no-pillar distribution. Starting from $\rho = 0.73$, we see that as ρ decreases to $\rho = 0.42$, there are still peaks evident in the array directions, but the probability that cell movements are aligned with the array directions is only 1.6 times greater than the no-pillar control distribution.

With these dramatic increases in directionality of motion we correspondingly observe an increase in persistence length as pillar array density is increased (fig. 5.3). To find the persistence length, we measured the angle β between cell displacements as a function of arc length $\boldsymbol{L}$. Using the typical definition of persistence length [109], we then measure the persistence length by fitting to

$$\langle cos(\beta_i) \rangle = e^{-\left(\frac{L_i}{P}\right)} \tag{5.1}$$

where $\boldsymbol{P}$ is the persistence length. For all low pillar densities $\rho \leq 0.13$, the path persistence is well-described by eqn. 5.1 with $P \approx 25\mu m$.

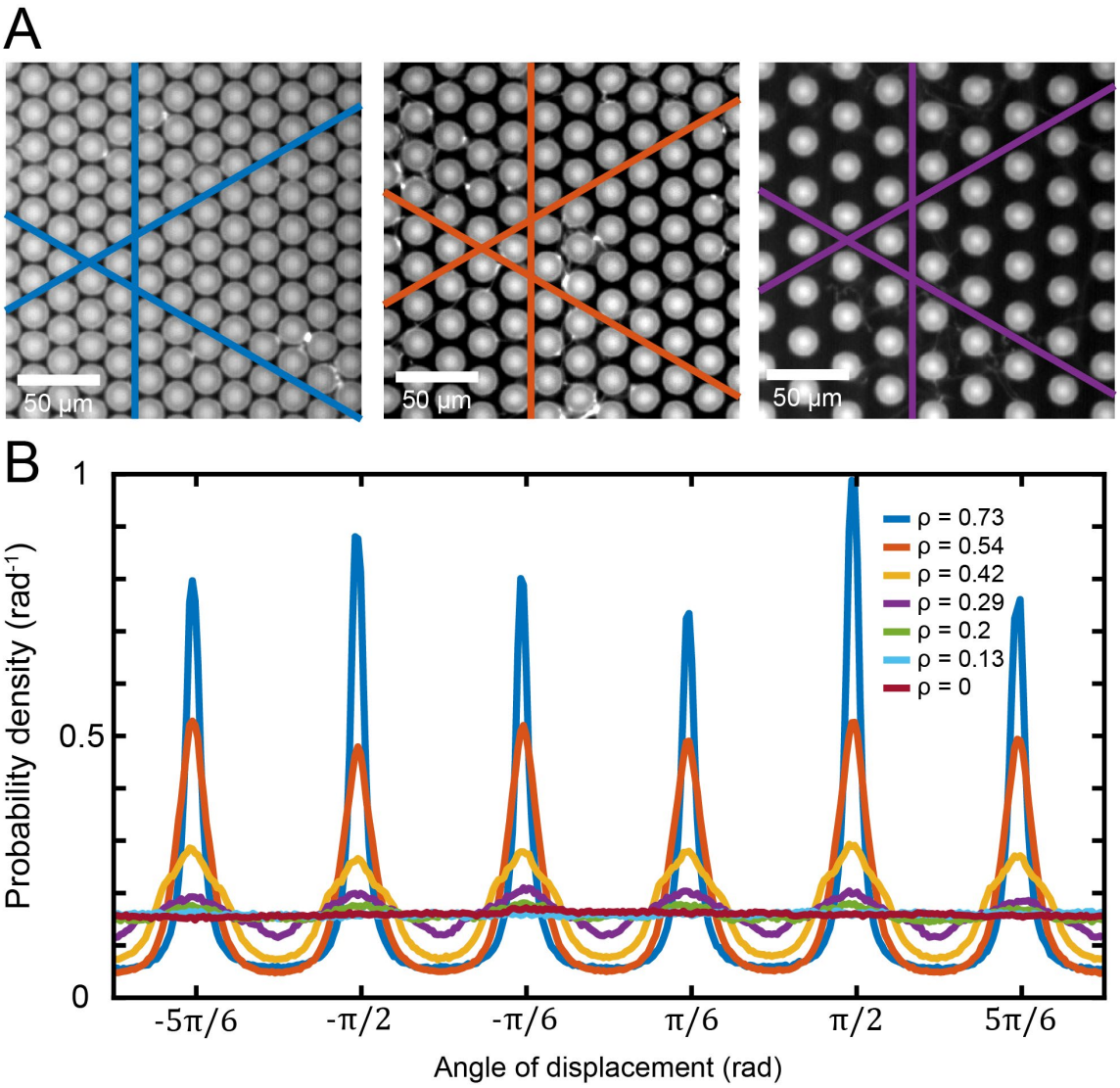

Figure 5.2: (A) Fluorescence images of three pillar arrays, $\rho = 0.73$, 0.54, and 0.29 with lines drawn along the directions of preferred motion. (B) Probability density function of the cell displacement angles in the image frame. Cell trajectories were smoothed, and the angles of cell displacements that were 20 μm apart in arclength were found. Clear peaks are present for trajectories in array densities $\rho \geq 0.2$, and below this density the angle distribution is flat and indistinguishable from trajectories in an open environment. The peaks are found at $\pm \pi/6$, $\pi/2$, and $5\pi/6$ radians, which correspond to the three lines of symmetry in the lattice.

This constant persistence length in addition to the similarities seen in MSD and the flat distribution in the direction of cell displacements lead us to conclude that at these lower densities, the pillars have little effect on overall cell trajectories. However, we found that for trajectories in the high-density pillar arrays ($\rho \geq 0.2$) the decay angular correlation fit poorly to a single exponential, but was well-described by the double exponential function

$$\langle cos(\beta_i) \rangle = Ce^{-\left(\frac{L_i}{P_1}\right)} + (1 - C)e^{-\left(\frac{L_i}{P_2}\right)} \quad (5.2)$$

which suggests that these trajectories have two characteristic length scales of motion (Fig. 5.3). The shorter persistence length P_1 appears to correspond to the gap widths between pillars. The longer persistence length P_2 corresponds to the highly persistent motion along the three array axes of relatively unimpeded motion (fig. 5.4). At the higher pillar densities we also see an oscillation in the angular correlation decay (fig. 5.5 B), which for $\rho = 0.73$ ($w = 2\mu m$) has a period of $21\mu m$ (fig. 5.5B) and for $\rho = 0.54$ ($w = 5\,\mu m$) has a period of $23\mu m$. The oscillation periods were found by examining peaks in the difference between the double exponential fit of the angle decay and the data. This oscillation period corresponds to two-times the distance cells travel between scattering off successive pillars. This value increases with gap width but is larger than the gap width because cells move to the next pillar following the tangent line to the previous pillar's surface (fig. 5.5A). Pairs of these forward scattering events create a 'zig-zag' pattern in cellular motion, which in turn causes a mild increase in their angle correlation that creates this added oscillation (fig. 5.5).

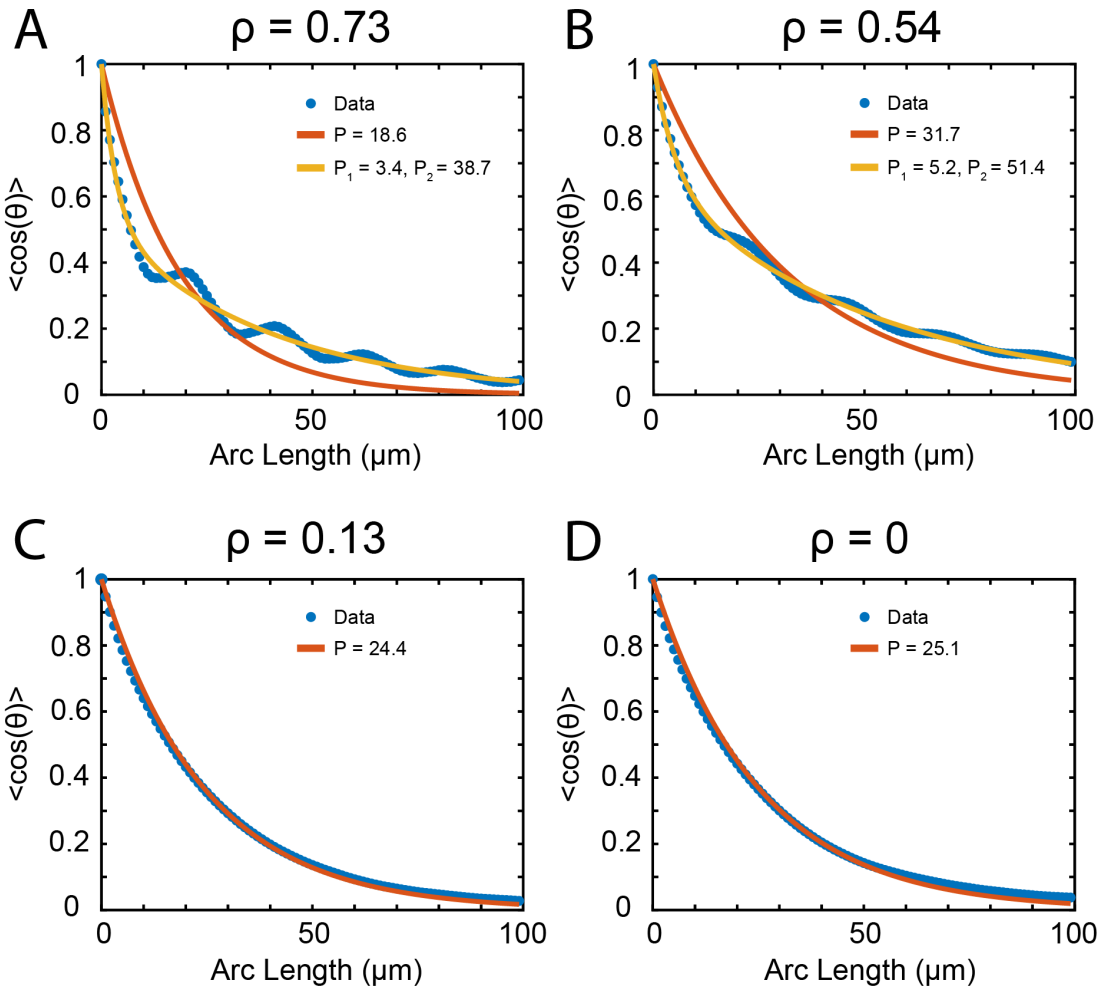

Figure 5.3: The mean cosine of the angle between displacement (unit) vectors β as a function of arc length between those vectors. We fit either a single (C and D) or double (A and B) exponential function to find the characteristic persistence length(s) of bacterial trajectories in arrays of four different pillar densities. For high densities (A and B), we see that single exponentials (red) fit poorly suggesting two characteristic lengths for the trajectories. The shorter persistence lengths (P_1) correspond to the typical distance traveled between consecutive pillar collisions which work to guide the cells in these high-density arrays. The oscillations seen in (A) and (B) are discussed in figure 5.4. (A) The best fit double exponential is $P_1 = 3.4, P_2 = 38.7$, and $C = 0.47$. (B) The best fit double exponential is $P_1 = 5.2, P_2 = 51.4$, and $C = 0.35$. (C) The best fit double exponential is $P_1 = 6.7, P_2 = 34.3, and C = 030$. (D) The best fit is $P = 25.1$. We see little variance for the pillar densities between $\rho = 0.42$ and $\rho = 0$.

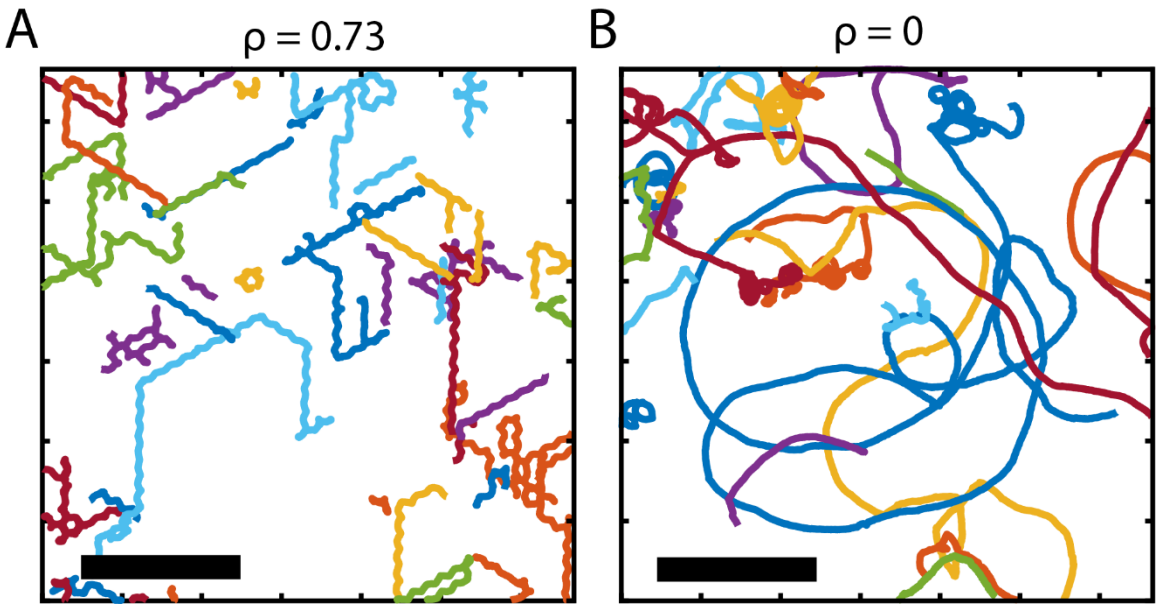

Figure 5.4: A random sampling of cell trajectories observed which were tracked for at least 10 seconds within the highest density pillar array (A) and no pillar array (B). (A) The cells move in a distinct 'zig-zag' pattern as cell-pillar collisions reorient the cell into consecutive pillars. The persistent motion of cells along the lines of symmetry of the pillar array can be clearly seen. (B) Cells which are hydrodynamically coupled to one of the planar surfaces can be seen moving in circular trajectories. Uncoupled cells move in typical run-and-tumble fashion. Scale bar 200 μm.

5.4 Conclusion

We have shown that over a broad range of obstacle densities, motion of cells in pillared environments remains largely unchanged from motion in non-pillared environments. The mean velocity of cells and the exponents characterizing the mean-squared displacement of cells and the crossover times between the exponents are constant across pillar density until extremely high pillar density ($\rho > 0.73$). This is in apparent disagreement with previous work that showed that even at relatively low ($\rho = 0.12$) obstacle densities there was a marked difference between MSD of cell trajectories [34].

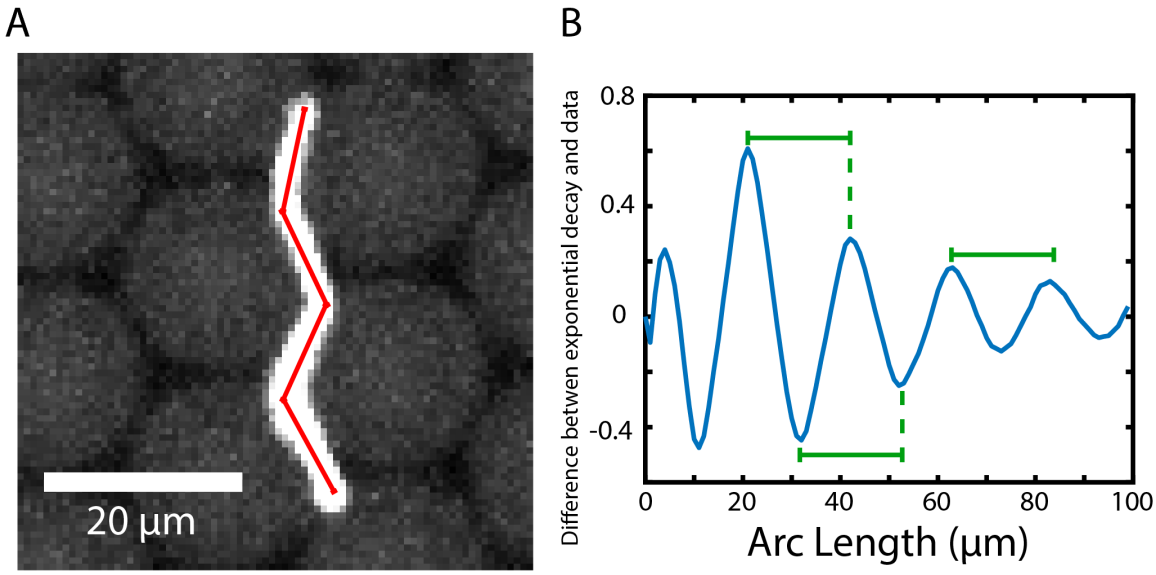

Figure 5.5: (A) A maximum intensity projection of 1.9 seconds of a cell moving in the typical 'zig-zag' pattern in a $\rho = 0.73$ array. The red line segments are all $10.5\mu m$ long. (B) The difference between the double exponential fit of the angle decay and the data shown separately in figure 5.2A. The green line segments are $21\mu m$ long and show that the period of the oscillation is double equal to two times the distance traveled by the cell between pillar interactions.

However, their study only looked at cell trajectories within a small area, a $25\mu m$ radius circle, and placed obstacles randomly. Their viewing area is too small to capture large-scale motion, including the full circular trajectories of cells which are coupled to the planar surface. Also, they studied the motion of cells when interacting with randomly placed obstacles. Our data shows that the direction of motion of cells was tightly bound by frequent interactions with pillars to the three axes of symmetry defined by the triangular lattice used to place pillars. Therefore, the placement of obstacles clearly has a clear effect on cell motion which could also explain differences between our results and previous

results. Given the observed strong directional preferences as a function of pillar density, it is unclear how such environments, with frequent forward scattering interactions, would affect the ability for cells to chemotax. In order to successfully execute a directed random walk, bacteria must modulate their tumble rate in response to multiple chemical measurements across time. Recent work has proposed that *E. coli* are able to decrease their tumble-rate in environments containing large obstacles (~50 μm sided squares or 50 μm diameter pillars) in order to increase their rates of favorable gradient ascent [27]. However, this study defined a "tumble" by observing cumulative angle difference and thus conflates circular motion due to hydrodynamic torque from the planar surfaces with 'true' flagellar tumbles. They also used square grids of pillars in a larger rectangular enclosure and our results suggest that array geometry plays a key role in directing cell motion.

CHAPTER VI

CONCLUSIONS AND FUTURE WORK

6.1 Motion of Microswimmers

The previous chapters described work on experiments and a novel method for microfluidic device creation, all of which point toward promising avenues of further work. This chapter will summarize the work presented in previous chapters and then describe future work related to their research directions. Generally, the work presented in this thesis examines the individual or collective motion of bacteria, how interactions with other cells or obstacles of similar size affect their motion, and the underlying physical mechanisms behind some of these interactions. While this work was done using bacteria, much of what was discussed has applications to other active-matter systems, especially abiotic microswimmers.

6.2 Collective Motion of Mixed Phenotype Populations

Chapter 2 described work exploring the high density collective motion of mixed motility-phenotypes of *Bacillus subtilis* to shed light on the effects that non-motile agents have on active-matter systems. This work was limited by an inability to precisely control the key variable of cell density, as well as limitations of image analysis. Our current image analysis techniques were unable to reliably identify and track single cells in these high density collectives, thankfully the dense packing of cells – with intensity variations linked

to cell positions – was amenable to extraction of quantitative information using Particle Image Velocimetry (PIV). With advances in machine-learning based image analysis techniques, robust single-cell tracking may be achievable even at these high densities. The resulting large volumes of high-resolution cell trajectory data would enable rigorous characterization of the effects of non-motile cells (or other objects) on collective motility. For instance, as a function of cell density and genotypic ratio one could: (i) probe individual cellular motions (of both genotypes) to calculate dispersal rates that differ by genotype, (ii) characterize and classify the 'phase diagram' of resulting motile behavior at the level of the group and the level of the individual, and (iii) examine the collective motion of other mixed-genotype populations that, for instance, vary morphological characteristics of cells.

6.3 Steric Interactions with Small Obstacles

Chapter 3 described a novel method for the creation of single-layer microfluidic devices that consisted of patterned photoresist chambers and features sealed by a thin layer of PDMS bonded to glass. This method allowed us to create devices with a number of unique properties, including increased feature resolution, resulting from the use of patterned photoresist, and massively increased size of stable, unsupported areas within the device as compared to typical soft lithography techniques. These devices were subsequently used to study the interactions between individual *Escherichia coli* and small, high-curvature obstacles. Chapter 4 described the main body of this work in which we acquired large-number high-resolution data of cell-pillar interactions. These data showed that for obstacle sizes a few cell lengths or less, hydrodynamic models fail to describe the interactions well, rather such scattering is well modeled as a purely steric interaction.

Importantly, while this work was done using *E. coli*, the experimental results and the corresponding model are likely generalizable to artificial and natural elongated pusher-type microswimmers, such as rod-shaped Janus particles or many other species of microorganism. Chapter 5 then described the results from our work studying the cumulative effects that these scattering interactions have on overall cell motility. We found that at high pillar densities, frequent scattering constrained cell motion along the axes of the triangular array of pillars, highlighting the importance of obstacle placement. Below these high densities, motion was dominated by typical run-and-tumble dynamics or hydrodynamic coupling to large planar surfaces, and thus was largely unaffected by the pillars.

The previously described experiments (chapters 2,4 and 5) and our ability to fabricate appropriate microfluidic devices (chapter 3) presents numerous opportunities for further study. First, our fabrication techniques allow us to create steric obstacles of nearly arbitrary shape across a wide range of sizes. With an experimental and data analysis process similar to Chapter 4, we could characterize – and potentially model – cell-object interactions across changes in object shape, size, and placement.. Specifically, we would start by examining interactions with negative curvature (concave) surfaces and probe the interplay between steric and hydrodynamic forces in such interactions – characterizing scattering processes and comparing to expanded versions of the sterics-only model. Second, we saw that the placement of pillars potently affects cell trajectories and persistence length (chapter 5). Our devices allow arbitrarily placement of pillars and thus enables quantitative measurements of the effects of obstacle placement on cell trajectories. Pillars could be positioned in various regular patterns or with different random placement algorithms to

mimic physical anisotripies found in natural systems - like wet soil or ocean particulates - thus enabling controlled observation of cell motility in artificial and controlled models of these natural environments. Additionally, we currently have a working prototype of a microfluidic device that creates a stable linear chemical gradient across a wide channel in which structures can be patterned. With these devices, the Ursell Lab plans to examine the effects of obstacle-bacteria interactions on the ability of cells to chemotax in physically heterogeneous environments, while varying gradient strength and structural parameters (i.e. size and placement of obstacles). High precision measurements of cellular flux up the nutrient gradient could be made with the same imaging and analysis used in Chapter 4 to reveal how object size, shape, and placement (among other parameters) affect chemotaxis. For instance, high resolution cell trajectory data could be used to distinguish flagellar tumbles from directional reorientations due to cell-surface interactions or angular diffusion. Data of this kind is currently unavailable and would help elucidate how cells chemotax in heterogenous environments as the adjustment of tumble rate is the key mechanism which enables chemotaxis [14], [110].

Our microfluidic devices can also be used for further experiments involving the high density collective motion of cells. Microfluidic devices provide precise control over cell density, which had been a key issue in our work presented in Chapter 2. The turbulent cellular flow of swarms likely is also substantially perturbed by obstacles of varied shape, size, and placement. By inoculating the population with a small number of fluorescent cells (as done by *Ariel et al.* [52]) one could measure the effects of such obstacles on the movement of individual cells within swarm, and similarly, PIV vector-field analysis could be used to measure the dependence of mixing Lyapunov exponents (a scalar measure of

mixing) on the shape, size and placement of obstacles.. Similarly, by doping the swarm with 20 *nm* diameter fluorescent tracer beads, the fluid flow can be quantitatively characterized by the same PIV algorithms. The developments that were made in device fabrication and cell tracking algorithms provide excellent opportunities for expanding on the research presented in this thesis. My thesis work generally studied interactions between the motion of self-propelled flagellated microorganisms and other cells and small obstacles of varying size. Due to their relatively simple behaviors, bacteria present an excellent model to study the physics of motion at low Reynolds number and further discoveries about the motion of self-propelled bacteria will lead to a more comprehensive understanding of bacterial microbiology.

REFERENCES CITED

[1] W. B. Whitman, D. C. Coleman, and W. J. Wiebe, “Prokaryotes: The unseen majority,” *Proc Natl Acad Sci U S A*, vol. 95, no. 12, pp. 6578–6583, Jun. 1998.

[2] N. Fierer, M. A. Bradford, and R. B. Jackson, “Toward an Ecological Classification of Soil Bacteria,” *Ecology*, vol. 88, no. 6, pp. 1354–1364, 2007, doi: 10.1890/05-1839.

[3] A. Barberán, K. S. Ramirez, J. W. Leff, M. A. Bradford, D. H. Wall, and N. Fierer, “Why are some microbes more ubiquitous than others? Predicting the habitat breadth of soil bacteria,” *Ecology Letters*, vol. 17, no. 7, pp. 794–802, 2014, doi: 10.1111/ele.12282.

[4] T. Shiozaki, M. Ijichi, T. Kodama, S. Takeda, and K. Furuya, “Heterotrophic bacteria as major nitrogen fixers in the euphotic zone of the Indian Ocean,” *Global Biogeochemical Cycles*, vol. 28, no. 10, pp. 1096–1110, 2014, doi: 10.1002/2014GB004886.

[5] M. Milici *et al.*, “Diversity and community composition of particle-associated and free-living bacteria in mesopelagic and bathypelagic Southern Ocean water masses: Evidence of dispersal limitation in the Bransfield Strait,” *Limnology and Oceanography*, vol. 62, no. 3, pp. 1080–1095, 2017, doi: 10.1002/lno.10487.

[6] R. Cord-Ruwisch, W. Kleinitz, and F. Widdel, “Sulfate-reducing Bacteria and Their Activities in Oil Production,” *Journal of Petroleum Technology*, vol. 39, no. 01, pp. 97–106, Jan. 1987, doi: 10.2118/13554-PA.

[7] K. Grond, B. K. Sandercock, A. Jumpponen, and L. H. Zeglin, “The avian gut microbiota: community, physiology and function in wild birds,” *Journal of Avian Biology*, vol. 49, no. 11, p. e01788, 2018, doi: 10.1111/jav.01788.

[8] R. E. Ley, C. A. Lozupone, M. Hamady, R. Knight, and J. I. Gordon, “Worlds within worlds: evolution of the vertebrate gut microbiota,” *Nat Rev Microbiol*, vol. 6, no. 10, pp. 776–788, Oct. 2008, doi: 10.1038/nrmicro1978.

[9] T. M. Nelson, T. L. Rogers, and M. V. Brown, “The Gut Bacterial Community of Mammals from Marine and Terrestrial Habitats,” *PLOS ONE*, vol. 8, no. 12, p. e83655, Dec. 2013, doi: 10.1371/journal.pone.0083655.

[10] M. Rajilić-Stojanović, “Function of the microbiota,” *Best Practice & Research Clinical Gastroenterology*, vol. 27, no. 1, pp. 5–16, Feb. 2013, doi: 10.1016/j.bpg.2013.03.006.

[11] N. Sabbuba, G. Hughes, and D. j. Stickler, “The migration of Proteus mirabilis and other urinary tract pathogens over Foley catheters,” *BJU International*, vol. 89, no. 1, pp. 55–60, Jan. 2002, doi: 10.1046/j.1464-410X.2002.02560.x.

[12] P. A. Tambyah, K. T. Halvorson, and D. G. Maki, “A Prospective Study of Pathogenesis of Catheter-Associated Urinary Tract Infections,” *Mayo Clinic Proceedings*, vol. 74, no. 2, pp. 131–136, Feb. 1999, doi: 10.4065/74.2.131.

[13] B. S. Lambert, V. I. Fernandez, and R. Stocker, “Motility drives bacterial encounter with particles responsible for carbon export throughout the ocean,” *Limnology and Oceanography Letters*, vol. 4, no. 5, pp. 113–118, 2019, doi: 10.1002/lol2.10113.

[14] H. C. Berg and D. A. Brown, “Chemotaxis in Escherichia coli analysed by Three-dimensional Tracking,” *Nature*, vol. 239, no. 5374, pp. 500–504, Oct. 1972, doi: 10.1038/239500a0.

[15] Marcos, H. C. Fu, T. R. Powers, and R. Stocker, “Bacterial rheotaxis,” *PNAS*, vol. 109, no. 13, pp. 4780–4785, Mar. 2012, doi: 10.1073/pnas.1120955109.

[16] E. Lauga, W. R. DiLuzio, G. M. Whitesides, and H. A. Stone, “Swimming in Circles: Motion of Bacteria near Solid Boundaries,” *Biophys J*, vol. 90, no. 2, pp. 400–412, Jan. 2006, doi: 10.1529/biophysj.105.069401.

[17] P. Galajda, J. Keymer, P. Chaikin, and R. Austin, “A Wall of Funnels Concentrates Swimming Bacteria,” *Journal of Bacteriology*, vol. 189, no. 23, pp. 8704–8707, Dec. 2007, doi: 10.1128/JB.01033-07.

[18] D. B. Kearns and R. Losick, “Swarming motility in undomesticated Bacillus subtilis,” *Molecular Microbiology*, vol. 49, no. 3, pp. 581–590, 2003, doi: 10.1046/j.1365-2958.2003.03584.x.

[19] E. M. Purcell, “Life at low Reynolds number,” *American Journal of Physics*, vol. 45, no. 1, pp. 3–11, Jan. 1977, doi: 10.1119/1.10903.

[20] O. Reynolds, “An Experimental Investigation of the Circumstances Which Determine Whether the Motion of Water Shall Be Direct or Sinuous, and of the Law of Resistance in Parallel Channels,” *Philosophical Transactions of the Royal Society of London*, vol. 174, pp. 935–982, 1883.

[21] R. M. Macnab, “Bacterial flagella rotating in bundles: a study in helical geometry,” *PNAS*, vol. 74, no. 1, pp. 221–225, Jan. 1977, doi: 10.1073/pnas.74.1.221.

[22] S. H. Larsen, R. W. Reader, E. N. Kort, W. W. Tso, and J. Adler, “Change in direction of flagellar rotation is the basis of the chemotactic response in Escherichia coli,” *Nature*, vol. 249, no. 452, pp. 74–77, May 1974, doi: 10.1038/249074a0.

[23] E. Lauga, “Bacterial Hydrodynamics,” *Annual Review of Fluid Mechanics*, vol. 48, no. 1, pp. 105–130, 2016, doi: 10.1146/annurev-fluid-122414-034606.

[24] R. M. Macnab, “How Bacteria Assemble Flagella,” *Annu. Rev. Microbiol.*, vol. 57, no. 1, pp. 77–100, Oct. 2003, doi: 10.1146/annurev.micro.57.030502.090832.

[25] N. C. Darnton, L. Turner, S. Rojevsky, and H. C. Berg, “On Torque and Tumbling in Swimming Escherichia coli,” *Journal of Bacteriology*, vol. 189, no. 5, pp. 1756–1764, Mar. 2007, doi: 10.1128/JB.01501-06.

[26] R. W. Sheldon, A. Prakash, and W. H. Sutcliffe, “The Size Distribution of Particles in the Ocean1,” *Limnology and Oceanography*, vol. 17, no. 3, pp. 327–340, 1972, doi: 10.4319/lo.1972.17.3.0327.

[27] S. Rashid *et al.*, “Adjustment in tumbling rates improves bacterial chemotaxis on obstacle-laden terrains,” *PNAS*, vol. 116, no. 24, pp. 11770–11775, Jun. 2019, doi: 10.1073/pnas.1816315116.

[28] K. Drescher, J. Dunkel, L. H. Cisneros, S. Ganguly, and R. E. Goldstein, “Fluid dynamics and noise in bacterial cell–cell and cell–surface scattering,” *PNAS*, vol. 108, no. 27, pp. 10940–10945, Jul. 2011, doi: 10.1073/pnas.1019079108.

[29] G. J. Hancock and M. H. A. Newman, “The self-propulsion of microscopic organisms through liquids,” *Proceedings of the Royal Society of London. Series A. Mathematical and Physical Sciences*, vol. 217, no. 1128, pp. 96–121, Mar. 1953, doi: 10.1098/rspa.1953.0048.

[30] O. Sipos, K. Nagy, R. Di Leonardo, and P. Galajda, “Hydrodynamic Trapping of Swimming Bacteria by Convex Walls,” *Phys. Rev. Lett.*, vol. 114, no. 25, p. 258104, Jun. 2015, doi: 10.1103/PhysRevLett.114.258104.

[31] S. E. Spagnolie, G. R. Moreno-Flores, D. Bartolo, and E. Lauga, “Geometric capture and escape of a microswimmer colliding with an obstacle,” *Soft Matter*, vol. 11, no. 17, pp. 3396–3411, 2015, doi: 10.1039/C4SM02785J.

[32] B. Zhang, Y. Ding, and X. Xu, “Active suspensions of bacteria and passive objects: a model for the near field pair dynamics,” *arXiv:2002.04693 [cond-mat, physics:physics]*, Feb. 2020, Accessed: Mar. 17, 2020. [Online]. Available: http://arxiv.org/abs/2002.04693.

[33] D. Takagi, J. Palacci, A. B. Braunschweig, M. J. Shelley, and J. Zhang, “Hydrodynamic capture of microswimmers into sphere-bound orbits,” *Soft Matter*, vol. 10, no. 11, pp. 1784–1789, Feb. 2014, doi: 10.1039/C3SM52815D.

[34] S. Makarchuk, V. C. Braz, N. A. M. Araújo, L. Ciric, and G. Volpe, “Enhanced propagation of motile bacteria on surfaces due to forward scattering,” *Nature Communications*, vol. 10, no. 1, Art. no. 1, Sep. 2019, doi: 10.1038/s41467-019-12010-1.

[35] F. J. Arriaga, B. Lowery, and M. D. Mays, “A FAST METHOD FOR DETERMINING SOIL PARTICLE SIZE DISTRIBUTION USING A LASER INSTRUMENT,” *Soil Science*, vol. 171, no. 9, pp. 663–674, Sep. 2006, doi: 10.1097/01.ss.0000228056.92839.88.

[36] T. H. Skaggs, L. M. Arya, P. J. Shouse, and B. P. Mohanty, “Estimating Particle-Size Distribution from Limited Soil Texture Data,” *Soil Science Society of America Journal*, vol. 65, no. 4, pp. 1038–1044, 2001, doi: 10.2136/sssaj2001.6541038x.

[37] A. Cavagna *et al.*, “Scale-free correlations in starling flocks,” *PNAS*, vol. 107, no. 26, pp. 11865–11870, Jun. 2010, doi: 10.1073/pnas.1005766107.

[38] W. Bialek *et al.*, “Statistical mechanics for natural flocks of birds,” *PNAS*, vol. 109, no. 13, pp. 4786–4791, Mar. 2012, doi: 10.1073/pnas.1118633109.

[39] A. Alma, A. Farji-Brener, and L. Elizalde, “Collective Response of Leaf-Cutting Ants to the Effects of Wind on Foraging Activity,” *The American Naturalist*, vol. 188, pp. 000–000, Sep. 2016, doi: 10.1086/688419.

[40] Y. Katz, K. Tunstrøm, C. C. Ioannou, C. Huepe, and I. D. Couzin, "Inferring the structure and dynamics of interactions in schooling fish," *PNAS*, vol. 108, no. 46, pp. 18720–18725, Nov. 2011, doi: 10.1073/pnas.1107583108.

[41] J. Buhl *et al.*, "From Disorder to Order in Marching Locusts," *Science*, vol. 312, no. 5778, pp. 1402–1406, Jun. 2006, doi: 10.1126/science.1125142.

[42] A. Sokolov and I. S. Aranson, "Physical Properties of Collective Motion in Suspensions of Bacteria," *Phys. Rev. Lett.*, vol. 109, no. 24, p. 248109, Dec. 2012, doi: 10.1103/PhysRevLett.109.248109.

[43] N. Verstraeten *et al.*, "Living on a surface: swarming and biofilm formation," *Trends in Microbiology*, vol. 16, no. 10, pp. 496–506, Oct. 2008, doi: 10.1016/j.tim.2008.07.004.

[44] R. M. Harshey, "Bees aren't the only ones: swarming in Gram-negative bacteria," *Molecular Microbiology*, vol. 13, no. 3, pp. 389–394, 1994, doi: 10.1111/j.1365-2958.1994.tb00433.x.

[45] D. B. Kearns, "A field guide to bacterial swarming motility," *Nature Reviews Microbiology*, vol. 8, no. 9, Art. no. 9, Sep. 2010, doi: 10.1038/nrmicro2405.

[46] S. Trinschek, K. John, and U. Thiele, "Modelling of surfactant-driven front instabilities in spreading bacterial colonies," *Soft Matter*, vol. 14, no. 22, pp. 4464–4476, Jun. 2018, doi: 10.1039/C8SM00422F.

[47] N. C. Caiazza, R. M. Q. Shanks, and G. A. O'Toole, "Rhamnolipids Modulate Swarming Motility Patterns of Pseudomonas aeruginosa," *Journal of Bacteriology*, vol. 187, no. 21, pp. 7351–7361, Nov. 2005, doi: 10.1128/JB.187.21.7351-7361.2005.

[48] M. Fauvart *et al.*, "Surface tension gradient control of bacterial swarming in colonies of Pseudomonas aeruginosa," *Soft Matter*, vol. 8, no. 1, pp. 70–76, Dec. 2011, doi: 10.1039/C1SM06002C.

[49] A. Yang, W. S. Tang, T. Si, and J. X. Tang, "Influence of Physical Effects on the Swarming Motility of Pseudomonas aeruginosa," *Biophys. J.*, vol. 112, no. 7, pp. 1462–1471, Apr. 2017, doi: 10.1016/j.bpj.2017.02.019.

[50] B. Rhodeland, K. Hoeger, and T. Ursell, “Bacterial surface motility is modulated by colony-scale flow and granular jamming,” *Journal of The Royal Society Interface*, vol. 17, no. 167, p. 20200147, Jun. 2020, doi: 10.1098/rsif.2020.0147.

[51] H. H. Wensink *et al.*, “Meso-scale turbulence in living fluids,” *PNAS*, vol. 109, no. 36, pp. 14308–14313, Sep. 2012, doi: 10.1073/pnas.1202032109.

[52] G. Ariel, A. Rabani, S. Benisty, J. D. Partridge, R. M. Harshey, and A. Be’er, “Swarming bacteria migrate by Lévy Walk,” *Nature Communications*, vol. 6, no. 1, Art. no. 1, Sep. 2015, doi: 10.1038/ncomms9396.

[53] V. Zaburdaev, S. Denisov, and J. Klafter, “L\’evy walks,” *Rev. Mod. Phys.*, vol. 87, no. 2, pp. 483–530, Jun. 2015, doi: 10.1103/RevModPhys.87.483.

[54] A. Be’er and R. M. Harshey, “Collective Motion of Surfactant-Producing Bacteria Imparts Superdiffusivity to Their Upper Surface,” *Biophys J*, vol. 101, no. 5, pp. 1017–1024, Sep. 2011, doi: 10.1016/j.bpj.2011.07.019.

[55] A. Be’er *et al.*, “A phase diagram for bacterial swarming,” *Communications Physics*, vol. 3, no. 1, Art. no. 1, Apr. 2020, doi: 10.1038/s42005-020-0327-1.

[56] B. Ilkanaiv, D. B. Kearns, G. Ariel, and A. Be’er, “The effect of cell aspect ratio on swarming bacteria,” *Phys Rev Lett*, vol. 118, no. 15, p. 158002, Apr. 2017, doi: 10.1103/PhysRevLett.118.158002.

[57] J. V. McArthur, D. A. Kovacic, and M. H. Smith, “Genetic diversity in natural populations of a soil bacterium across a landscape gradient,” *PNAS*, vol. 85, no. 24, pp. 9621–9624, Dec. 1988, doi: 10.1073/pnas.85.24.9621.

[58] J. M. Smith, N. H. Smith, M. O’Rourke, and B. G. Spratt, “How clonal are bacteria?,” *Proc Natl Acad Sci USA*, vol. 90, no. 10, p. 4384, May 1993, doi: 10.1073/pnas.90.10.4384.

[59] O. Feinerman, I. Pinkoviezky, A. Gelblum, E. Fonio, and N. S. Gov, “The physics of cooperative transport in groups of ants,” *Nature Physics*, vol. 14, no. 7, Art. no. 7, Jul. 2018, doi: 10.1038/s41567-018-0107-y.

[60] R. Gallotti and D. R. Chialvo, “How ants move: individual and collective scaling properties,” *Journal of The Royal Society Interface*, vol. 15, no. 143, p. 20180223, Jun. 2018, doi: 10.1098/rsif.2018.0223.

[61] O. Sipos, K. Nagy, and P. Galajda, “Patterns of Collective Bacterial Motion in Microfluidic Devices,” *Chem.Biochem.Eng.Q.*, vol. 28, no. 2, pp. 233–240, 2014, doi: 10.15255/CABEQ.2013.1935.

[62] F. Peruani, J. Starruß, V. Jakovljevic, L. Søgaard-Andersen, A. Deutsch, and M. Bär, “Collective Motion and Nonequilibrium Cluster Formation in Colonies of Gliding Bacteria,” *Phys. Rev. Lett.*, vol. 108, no. 9, p. 098102, Feb. 2012, doi: 10.1103/PhysRevLett.108.098102.

[63] H. P. Zhang, A. Be’er, E.-L. Florin, and H. L. Swinney, “Collective motion and density fluctuations in bacterial colonies,” *PNAS*, vol. 107, no. 31, pp. 13626–13630, Aug. 2010, doi: 10.1073/pnas.1001651107.

[64] T. Ishikawa, N. Yoshida, H. Ueno, M. Wiedeman, Y. Imai, and T. Yamaguchi, “Energy Transport in a Concentrated Suspension of Bacteria,” *Phys. Rev. Lett.*, vol. 107, no. 2, p. 028102, Jul. 2011, doi: 10.1103/PhysRevLett.107.028102.

[65] L. H. Cisneros, J. O. Kessler, S. Ganguly, and R. E. Goldstein, “Dynamics of swimming bacteria: Transition to directional order at high concentration,” *Phys. Rev. E*, vol. 83, no. 6, p. 061907, Jun. 2011, doi: 10.1103/PhysRevE.83.061907.

[66] A. Sokolov, I. S. Aranson, J. O. Kessler, and R. E. Goldstein, “Concentration Dependence of the Collective Dynamics of Swimming Bacteria,” *Phys. Rev. Lett.*, vol. 98, no. 15, p. 158102, Apr. 2007, doi: 10.1103/PhysRevLett.98.158102.

[67] H. Wioland, F. G. Woodhouse, J. Dunkel, J. O. Kessler, and R. E. Goldstein, “Confinement Stabilizes a Bacterial Suspension into a Spiral Vortex,” *Phys. Rev. Lett.*, vol. 110, no. 26, p. 268102, Jun. 2013, doi: 10.1103/PhysRevLett.110.268102.

[68] H. Wioland, F. G. Woodhouse, J. Dunkel, and R. E. Goldstein, “Ferromagnetic and antiferromagnetic order in bacterial vortex lattices,” *Nature Physics*, vol. 12, no. 4, Art. no. 4, Apr. 2016, doi: 10.1038/nphys3607.

[69] H. Wioland, E. Lushi, and R. E. Goldstein, “Directed collective motion of bacteria under channel confinement,” *New J. Phys.*, vol. 18, no. 7, p. 075002, Jul. 2016, doi: 10.1088/1367-2630/18/7/075002.

[70] W. Thielicke and E. Stamhuis, “PIVlab – Towards User-friendly, Affordable and Accurate Digital Particle Image Velocimetry in MATLAB,” *Journal of Open Research Software*, vol. 2, no. 1, Art. no. 1, Oct. 2014, doi: 10.5334/jors.bl.

[71] W. Thielicke, “The flapping flight of birds: Analysis and application,” [S.n.], 2014.

[72] J. Dunkel, S. Heidenreich, K. Drescher, H. H. Wensink, M. Bär, and R. E. Goldstein, "Fluid Dynamics of Bacterial Turbulence," *Phys. Rev. Lett.*, vol. 110, no. 22, p. 228102, May 2013, doi: 10.1103/PhysRevLett.110.228102.

[73] M. M. Salek, F. Carrara, V. Fernandez, J. S. Guasto, and R. Stocker, "Bacterial chemotaxis in a microfluidic T-maze reveals strong phenotypic heterogeneity in chemotactic sensitivity," *Nature Communications*, vol. 10, no. 1, Art. no. 1, Apr. 2019, doi: 10.1038/s41467-019-09521-2.

[74] Y. Liu *et al.*, "Microfluidics-based assay on the effects of microenvironmental geometry and aqueous flow on bacterial adhesion behaviors," *Journal of Pharmaceutical Analysis*, vol. 1, no. 3, pp. 175–183, Aug. 2011, doi: 10.1016/j.jpha.2011.06.001.

[75] M. S. D. Wykes *et al.*, "Guiding microscale swimmers using teardrop-shaped posts," *Soft Matter*, vol. 13, no. 27, pp. 4681–4688, Jul. 2017, doi: 10.1039/C7SM00203C.

[76] A. Sokolov, M. M. Apodaca, B. A. Grzybowski, and I. S. Aranson, "Swimming bacteria power microscopic gears," *PNAS*, vol. 107, no. 3, pp. 969–974, Jan. 2010, doi: 10.1073/pnas.0913015107.

[77] T. Kaya and H. Koser, "Direct Upstream Motility in Escherichia coli," *Biophysical Journal*, vol. 102, no. 7, pp. 1514–1523, Apr. 2012, doi: 10.1016/j.bpj.2012.03.001.

[78] E. Altshuler *et al.*, "Flow-controlled densification and anomalous dispersion of E. coli through a constriction," *Soft Matter*, vol. 9, no. 6, pp. 1864–1870, 2013, doi: 10.1039/C2SM26460A.

[79] R. Rusconi, J. S. Guasto, and R. Stocker, "Bacterial transport suppressed by fluid shear," *Nature Physics*, vol. 10, no. 3, Art. no. 3, Mar. 2014, doi: 10.1038/nphys2883.

[80] G. L. Miño *et al.*, "*E coli* Accumulation behind an Obstacle," *Advances in Microbiology*, vol. 08, no. 06, Art. no. 06, Jun. 2018, doi: 10.4236/aim.2018.86030.

[81] E. Secchi *et al.*, "The effect of flow on swimming bacteria controls the initial colonization of curved surfaces," *bioRxiv*, p. 866491, Dec. 2019, doi: 10.1101/866491.

[82] H. Mao, P. S. Cremer, and M. D. Manson, "A sensitive, versatile microfluidic assay for bacterial chemotaxis," *PNAS*, vol. 100, no. 9, pp. 5449–5454, Apr. 2003, doi: 10.1073/pnas.0931258100.

[83] J. Atencia, J. Morrow, and L. E. Locascio, “The microfluidic palette: A diffusive gradient generator with spatio-temporal control,” *Lab on a Chip*, vol. 9, no. 18, pp. 2707–2714, 2009, doi: 10.1039/B902113B.

[84] K. Nagy *et al.*, “Microfluidic study of the chemotactic response of Escherichia coli to amino acids, signaling molecules and secondary metabolites,” *Biomicrofluidics*, vol. 9, no. 4, Jul. 2015, doi: 10.1063/1.4926981.

[85] Y. Xia and G. M. Whitesides, “Soft Lithography,” *Angewandte Chemie International Edition*, vol. 37, no. 5, pp. 550–575, Mar. 1998, doi: 10.1002/(SICI)1521-3773(19980316)37:5<550::AID-ANIE550>3.0.CO;2-G.

[86] J. C. McDonald and G. M. Whitesides, “Poly(dimethylsiloxane) as a Material for Fabricating Microfluidic Devices,” *Acc. Chem. Res.*, vol. 35, no. 7, pp. 491–499, Jul. 2002, doi: 10.1021/ar010110q.

[87] Z. Wang, A. A. Volinsky, and N. D. Gallant, “Crosslinking effect on polydimethylsiloxane elastic modulus measured by custom-built compression instrument,” *J. Appl. Polym. Sci.*, vol. 131, no. 22, p. n/a-n/a, Nov. 2014, doi: 10.1002/app.41050.

[88] M. A. Unger, H.-P. Chou, T. Thorsen, A. Scherer, and S. R. Quake, “Monolithic Microfabricated Valves and Pumps by Multilayer Soft Lithography,” *Science*, vol. 288, no. 5463, pp. 113–116, Apr. 2000, doi: 10.1126/science.288.5463.113.

[89] H. Bruus, *Theoretical Microfluidics*. 2008.

[90] “Microfluidics and Nanofluidics Handbook: Fabrication, Implementation, and Applications,” *CRC Press*. https://www.routledge.com/Microfluidics-and-Nanofluidics-Handbook-Fabrication-Implementation-and/Mitra-Chakraborty/p/book/9781138072381 (accessed Jun. 04, 2020).

[91] E. O. Budrene and H. C. Berg, “Dynamics of formation of symmetrical patterns by chemotactic bacteria,” *Nature*, vol. 376, no. 6535, Art. no. 6535, Jul. 1995, doi: 10.1038/376049a0.

[92] M. Molaei, M. Barry, R. Stocker, and J. Sheng, “Failed Escape: Solid Surfaces Prevent Tumbling of Escherichia coli,” *Phys. Rev. Lett.*, vol. 113, no. 6, p. 068103, Aug. 2014, doi: 10.1103/PhysRevLett.113.068103.

[93] A. E. Patteson, A. Gopinath, M. Goulian, and P. E. Arratia, “Running and tumbling with E. coli in polymeric solutions,” *Scientific Reports*, vol. 5, no. 1, Art. no. 1, Oct. 2015, doi: 10.1038/srep15761.

[94] A. Persat, H. A. Stone, and Z. Gitai, “The curved shape of Caulobacter crescentus enhances surface colonization in flow,” *Nature Communications*, vol. 5, no. 1, Art. no. 1, May 2014, doi: 10.1038/ncomms4824.

[95] M. C. van Loosdrecht, J. Lyklema, W. Norde, and A. J. Zehnder, “Influence of interfaces on microbial activity.,” *Microbiology and Molecular Biology Reviews*, vol. 54, no. 1, pp. 75–87, Mar. 1990.

[96] M. Quirynen and C. M. L. Bollen, “The influence of surface roughness and surface-free energy on supra- and subgingival plaque formation in man,” *Journal of Clinical Periodontology*, vol. 22, no. 1, pp. 1–14, 1995, doi: 10.1111/j.1600-051X.1995.tb01765.x.

[97] J. Katuri, D. Caballero, R. Voituriez, J. Samitier, and S. Sanchez, “Directed Flow of Micromotors through Alignment Interactions with Micropatterned Ratchets,” *ACS Nano*, vol. 12, no. 7, pp. 7282–7291, Jul. 2018, doi: 10.1021/acsnano.8b03494.

[98] A. Kaiser, H. H. Wensink, and H. Löwen, “How to Capture Active Particles,” *Phys. Rev. Lett.*, vol. 108, no. 26, p. 268307, Jun. 2012, doi: 10.1103/PhysRevLett.108.268307.

[99] S. E. Hulme *et al.*, “Using ratchets and sorters to fractionate motile cells of Escherichia coli by length,” *Lab on a Chip*, vol. 8, no. 11, pp. 1888–1895, 2008, doi: 10.1039/B809892A.

[100] R. Mok, J. Dunkel, and V. Kantsler, “Geometric control of bacterial surface accumulation,” *Phys. Rev. E*, vol. 99, no. 5, p. 052607, May 2019, doi: 10.1103/PhysRevE.99.052607.

[101] A. Dehkharghani, N. Waisbord, J. Dunkel, and J. S. Guasto, “Bacterial scattering in microfluidic crystal flows reveals giant active Taylor–Aris dispersion,” *PNAS*, vol. 116, no. 23, pp. 11119–11124, Jun. 2019, doi: 10.1073/pnas.1819613116.

[102] P. D. Frymier, R. M. Ford, H. C. Berg, and P. T. Cummings, “Three-dimensional tracking of motile bacteria near a solid planar surface,” *PNAS*, vol. 92, no. 13, pp. 6195–6199, Jun. 1995, doi: 10.1073/pnas.92.13.6195.

[103] F. Qi *et al.*, “Soil particle size distribution characteristics of different land-use types in the Funiu mountainous region,” *Soil and Tillage Research*, vol. 184, pp. 45–51, Dec. 2018, doi: 10.1016/j.still.2018.06.011.

[104] E. Lushi, H. Wioland, and R. E. Goldstein, “Fluid flows created by swimming bacteria drive self-organization in confined suspensions,” *PNAS*, vol. 111, no. 27, pp. 9733–9738, Jul. 2014, doi: 10.1073/pnas.1405698111.

[105] D. Takagi, A. B. Braunschweig, J. Zhang, and M. J. Shelley, “Dispersion of Self-Propelled Rods Undergoing Fluctuation-Driven Flips,” *Phys. Rev. Lett.*, vol. 110, no. 3, p. 038301, Jan. 2013, doi: 10.1103/PhysRevLett.110.038301.

[106] D. B. Weibel and G. M. Whitesides, “Applications of microfluidics in chemical biology,” *Curr Opin Chem Biol*, vol. 10, no. 6, pp. 584–591, Dec. 2006, doi: 10.1016/j.cbpa.2006.10.016.

[107] J. B. Corliss *et al.*, “Submarine Thermal Springs on the Galápagos Rift,” *Science*, vol. 203, no. 4385, pp. 1073–1083, Mar. 1979, doi: 10.1126/science.203.4385.1073.

[108] G. J. Dick, “The microbiomes of deep-sea hydrothermal vents: distributed globally, shaped locally,” *Nature Reviews Microbiology*, vol. 17, no. 5, Art. no. 5, May 2019, doi: 10.1038/s41579-019-0160-2.

[109] D. Feldman, “The theory of polymer dynamics, by M. Doi and S. F. Edwards, the Clarendon Press, Oxford University Press, New York, 1986, 391 pp. Price: $78.50.,” *Journal of Polymer Science Part C: Polymer Letters*, vol. 27, no. 7, pp. 239–240, 1989, doi: 10.1002/pol.1989.140270706.

[110] D. A. Brown and H. C. Berg, “Temporal Stimulation of Chemotaxis in Escherichia coli,” *Proceedings of the National Academy of Sciences*, vol. 71, no. 4, pp. 1388–1392, Apr. 1974, doi: 10.1073/pnas.71.4.1388.